Stony Brook University

Development of narrow gap semiconductor materials and devices

for optoelectronic applications

A Dissertation Presented

by

Ding Wang

to

The Graduate School

in Partial Fulfillment of the

Requirements

for the Degree of

Doctor of Philosophy

in

Electrical Engineering

(Semiconductor Devices and Quantum Electronics)

Stony Brook University

August 2013

Stony Brook University

The Graduate School

Ding Wang

We, the dissertation committee for the above candidate for the

Doctor of Philosophy degree, hereby recommend

acceptance of this dissertation.

Gregory Belenky – Dissertation Advisor
Professor, Electrical and Computer Engineering

Dmitry Donetsky - Dissertation Co-Advisor
Associate Professor, Electrical and Computer Engineering

Ridha Kamoua - Chairperson of Defense
Associate Professor, Electrical and Computer Engineering

Leon Shterengas
Associate Professor, Electrical and Computer Engineering

David Hwang
Assistant Professor, Electrical and Computer Engineering

This dissertation is accepted by the Graduate School

Charles Taber
Interim Dean of the Graduate School

Abstract of the Dissertation

Development of narrow gap semiconductor materials and devices for optoelectronic applications

by

Ding Wang

Doctor of Philosophy

in

Electrical Engineering

(Semiconductor Devices and Quantum Electronics)

Stony Brook University

2013

Mid-wave to long-wave infrared (3~12 μm in wavelength) optoelectronic devices have broad applications in gas sensing, molecular spectroscopy, imaging, environmental, industrial monitoring, etc. This work aims to explore new III-V materials and heterostructures to develop light emitting devices and detectors for the infrared spectral region.

Optical properties of dilute nitride GaSbN and InAsN materials were investigated. We observed strong bandgap reduction with increasing nitrogen incorporation. GaSbN with 1.4% of nitrogen showed 300 meV narrower bandgap than GaSb; for InAsN the bandgap energy was reduced by 150 meV with nitrogen incorporation up to 2.25%. The carrier lifetimes within the picoseconds - nanoseconds range were measured for GaSbN and InAsN.

$InAs_{1-x}Sb_x$ alloys have the smallest bandgap energies within conventional III-V semiconductors. We demonstrated that growing compositionally graded buffers (Ga(Al)InSb on

GaSb substrates) allows the fabrication of bulk unstrained and unrelaxed $InAs_{1-x}Sb_x$ layers with band gap energy as low as 120 meV. Photoluminescence spectra (5 -10 μm) and minority carrier lifetimes (up to 250 ns) were measured.

Light emitting diodes (LEDs) and photodetectors were fabricated using $InAs_{1-x}Sb_x$ alloys. LEDs with x = 0.2 and x = 0.4 demonstrated output powers of 90 μW at 5 μm and 8 μW at 8 μm respectively, at the temperature of 80 K. Barrier type photodetectors with $InAs_{1-x}Sb_x$ (x = 0.4) absorber layer and AlInSb barrier were fabricated. Front side illuminated detectors with 1 μm thick absorber demonstrated an external quantum efficiency of 18 % at 8 μm at 150 K.

Table of Contents

List of Figures

Figure 3.2: AFM amplitude images measured over 50 by 50 μm area for samples with $InAs_{0.8}Sb_{0.2}$ layer grown on (a) GaInSb buffer and (b) AlGaInSb buffer; (c) shows the enlarged image (3 by 3 μm) of sample (b).

Figure 3.3: (a) Symmetric (004) RSM taken at the azimuth angle emphasizing the tilt in the epi-layers; (b) (004) RSM taken at the azimuth angle minimizing the tilt in the epi-layers; (c) dependence of the measured tilt angle as a function of the azimuth angle; (d) asymmetric (335) RSM taken at azimuth angle equal to 90˚. Solid line denotes the location of 335 reflexes corresponding to fully relaxed material with lattice parameter gradually increasing from that of GaSb. Dashed line denotes the location of 335 reflexes of the material with further increasing native lattice parameter but grown pseudomorphically to the top of fully relaxed section.

Figure 3.4: (a) PL spectra from $InAs_{0.8}Sb_{0.2}$ sample grown on AlGaInSb buffer at 13 K, 150 K and 300 K under an excitation power of 0.5W. (b) PL spectra from $InAs_{0.56}Sb_{0.44}$ layer grown on AlGaInSb buffer and long-wave InAs/GaSb superlattices grown on GaSb substrate at 13 K under an excitation of 0.1 W. The PL was excitation by a Nd:YAG laser with a beam diameter of about 0.5 mm.

Figure 3.5: Absorption and PL spectra measured at 150 K for (a) $InAs_{0.8}Sb_{0.2}$ and (b) $InAs_{0.7}Sb_{0.3}$. The PL was excited by a 970-nm laser diode at a power of 400 mW; the excitation area was 2.5 x 10^{-3} cm^2. The distortion near 0.29 eV was caused by CO2 absorption.

Figure 3.6: Dependence of 13K PL maxima on composition X in InAs1-XSbX epitaxial layers: InAs epilayer grown on InAs substrate (triangle), InAsSb0.08 epilayer grown lattice matched to GaSb substrate (circle), InAs1-XSbX epilayers grown on AlGaInSb buffers (squares) on GaSb substrate, InSb epilayers grown on InSb substrate (inverted triangles).

Figure 3.7: Carrier lifetime measurements at T= 77 K on a 1-μm-thick $InAs_{0.8}Sb_{0.2}$ layer grown on an AlGaInSb buffer on a GaSb substrate. (a) The PL responses and fits are presented for continuous wave excitation power levels of 0.8, 1, 1.4, 3 and 5 mW from bottom to top, respectively. The PL was excited at the wavelength of 1.31 μm, and the excitation area was 2×10^{-3} cm^2 FWHM. (b) The reciprocal carrier lifetime is plotted versus continuous–wave excitation power density.

Acknowledgments

I would like to thank many people who have helped me through the completion of this dissertation.

To all the past and current members of the Optoelectronics Group at Stony Brook University that I have been privileged enough to work with. Thanks for the help, support and friendship over the past six years I have spent here.

I wish to express my deepest gratitude to my advisers, Professor Gregory Belenky and Professor Dmitry Donetsky. Without their support and guidance this work could not be accomplished.

I would like to show my appreciation to Professor Leon Shterengas, Dr. Gela Kipshidze, Dr. Sergey Suchalkin, Dr. Stefan Svensson and Dr. Wendy Sarney for their insightful suggestions and many helpful discussions.

The last and most important thanks are dedicated to my family - my parents and my wife - for their love, support and belief in me.

Journal Publications

1. **D. Wang**, D. Donetsky, G. Kipshidze, Y. Lin, L. Shterengas, G. Belenky, W. L. Sarney, and S. P. Svensson, "Metamorphic InAsSb-based barrier photodetectors for the long wave infrared region," Appl. Phys. Lett. 103, 051120 (2013).
2. G. Belenky, **D. Wang**, Y. Lin, D. Donetsky, G. Kipshidze, L. Shterengas, D. Westerfeld, W. L. Sarney, and S. P. Svensson, "Metamorphic InAsSb/AlInAsSb heterostructures for optoelectronic applications," Appl. Phys. Lett. 102, 111108 (2013).
3. S.P. Svensson, W.L. Sarny, H. Hier, Y. Lin, **D. Wang**, D. Donetsky, L. Shterengas, G. Kipshidze, G. Belenky, "Band gap of $InAs_{1-x}Sb_x$ with native lattice constant," Phys. Rev. B 86, 245205 (2012).
4. **D. Wang**, D. Donetsky, S. Jung, G. Belenky, "Carrier lifetime measurements in long-wave infrared InAs/GaSb superlattices under low excitation conditions", J. Electron. Mater. 41, 3027 (2012).
5. **D. Wang**, D. Donetsky, Y. Lin, G. Kipshidze, L. Shterengas, G. Belenky, W. L. Sarney, S. P. Svensson, "$InAs_{1-x}Sb_x$ alloys with native lattice parameters grown on compositionally graded buffers: structural and optical properties," Int. J. High Speed Electron. Syst. 21, 1250013 (2012).
6. T. Hosoda, **D. Wang**, G. Kipshidze, W. L. Sarney, L. Shterengas, G. Belenky, "3 μm diode layers grown on (Al)GaInSb compositionally graded metamorphic buffer layers", Semicond. Sci. Technol. 27, 055011 (2012).
7. S.P. Svensson, H. Hier, W.L. Sarney, D. Donetsky, **D. Wang**, G. Belenky, "Molecular beam epitaxy control and photoluminescence properties of InAsBi," J. Vac. Sci. Technol. B 30, 02B109 (2012).
8. W.L. Sarney, S.P. Svensson, H. Hier, G. Kipshidze, D. Donetsky, **D. Wang**, L. Shterengas, G. Belenky, "Structural and luminescent properties of bulk InAsSb," J. Vac. Sci. Technol. B 30, 02B105 (2012).
9. G. Belenky, D. Donetsky, G. Kipshidze, **D. Wang**, L. Shterengas, W.L. Sarney and S.P. Svensson, "Properties of unrelaxed $InAs_{1-X}Sb_X$ alloys grown on compositionally graded buffers," Appl. Phys. Lett. 99, 141116 (2011).
10. S.P. Svensson, D. Donetsky, **D. Wang**, H. Hier, F.J. Crowne, G. Belenky, "Growth of type II strained layer superlattice, bulk InAs and GaSb materials for minority lifetime characterization," J. Cryst. Growth 334, 103 (2011).
11. **D. Wang**, S.P. Svensson, L. Shterengas, G. Belenky, "Near band edge optical absorption and photoluminescence dynamics in bulk InAsN dilute-nitride materials," J. Cryst. Growth 312, 2705 (2010).

12. G. Belenky, L. Shterengas, **D. Wang**, G. Kipshidze and L. Vorobjev, "Continuous wave operated 3.2 μm type-I quantum-well diode lasers with the quinary waveguide layer," Semicond. Sci. Technol. 24, 115013 (2009).
13. **D. Wang**, S.P. Svensson, L. Shterengas, G. Belenky, C.S. Kim, I. Vurgaftman and J.R. Meyer, "Band edge optical transitions in dilute-nitride GaNSb," J. Appl. Phys. 105, 014904 (2009).
14. J.Y.T. Huang, L.J. Mawst, S. Jha, T.F. Kuech, **D. Wang**, L. Shterengas, G. Belenky, J.R. Meyer and I. Vurgaftman, "MOVPE growth of Ga(As)SbN on GaSb substrates," J. Cryst. Growth 310, 4839 (2008).

Chapter 1 Introduction

Interest in infrared technology arises from the unique properties of infrared radiation, or so-called infrared light. For example, objects warmer than the ambient temperature generally emit their energy as infrared radiation; especially, human body emits at a peak wavelength about 10 μm. Typical applications in this category include thermography, night vision, remote temperature sensing, missile tracking, etc. Another interesting property of infrared radiation is the atmospheric window at about 3-5 μm and 8-14 μm. Infrared light at these wavelengths can travel on earth or to space without substantial absorption, and thus such emitters and detectors can be or are used in communications, remote sensing, astronomy, etc. Infrared emitters and detectors are also used in gas sensing because some atmospheric molecules, such as carbon dioxide, methane, ozone, absorb infrared light at specific wavelengths in the atmospheric window. Infrared spectroscopy is another important scientific, medical and industrial application since molecules and crystals often absorb or sometimes emit light in the infrared region. To fulfill the requirements of these applications, infrared emitters and detectors should possess one or more of the following attributes: efficient, stable, small in size, low power consumption and low cost.

III-V semiconductors are suitable materials for the development of infrared optoelectronic devices. Figure 1.1 shows the plot of band gap energy/wavelength versus lattice constant of commonly used III-V binary alloys (using parameters from Ref [1]). The band gap energy of bulk III-V binaries ranges from about 0.24 eV to more than 3 eV, covering a wavelength region from visible to mid-wave infrared (MWIR). With sophisticated band gap engineering, i.e., superlattice structures [2], interband [3] and intersubband quantum cascade structures [4], the optical wavelength of III-V semiconductors can be extended beyond long-wave infrared (LWIR) region.

This work is focused on the development of III-V semiconductor materials and devices for the middle and long wave infrared applications. In the following part of the chapter, we will review the available III-V semiconductor materials, as well as the available optoelectronic devices based on III-V semiconductors. Chapter 2 presents our work on a new type of narrow band gap materials, namely dilute nitrides. Chapter 3 presents our effort on developing unrelaxed and unstrained InAsSb alloys (with native lattice constants) using lattice mismatched epitaxy. Chapter 4 extends this work and demonstrates light emitting diodes (LEDs) and photodetectors based on these InAsSb alloys. A summary and future works will be discussed in Chapter 5.

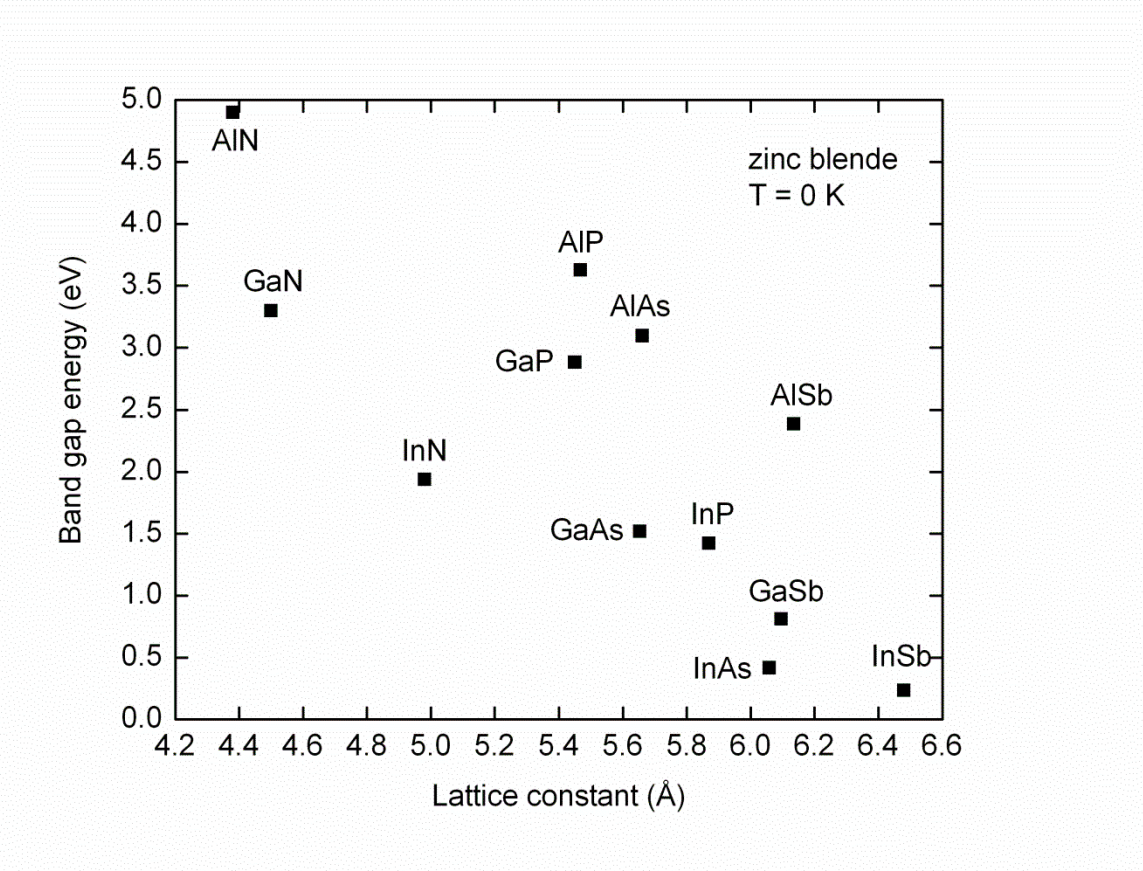

Figure 1.1: Direct band gap (Γ-valley) energy versus lattice constant for the zinc blende form of 12 III-V binary semiconductors (using parameters from Ref. [1]).

1.1 Narrow gap III-V semiconductor materials

Narrow gap semiconductor materials are those with band gap energies smaller than 1 eV, e.g. GaSb, InAs, and InSb as shown in Figure 1.1. This section will introduce the fundamental crystal structure and electronic band structure of these materials.

1.1.1 Crystal structure

Most of the III-V semiconductors (except some III-nitrides with wurtzite structure) have zinc blende crystal structure which consists of two interpenetrating face-centered-cube (FCC) lattices (displaced along the body diagonal of the cubic cell by one quarter the length of the diagonal), one having group-III atoms and the other having group-V atoms. Figure 1.2 shows the conventional unit cell of zinc blende structure. It can be considered as a FCC lattice with a basis,

noted by the arrow in the figure. Next we will go through some fundamental concepts in crystallography, including Bravais lattice, primitive vectors, reciprocal lattice, and Miller indices.

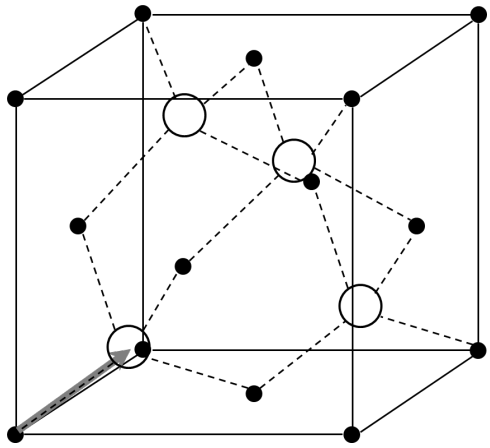

Figure 1.2: Conventional unit cell of the zinc blende structure. The dots and circles denote either III-group or V-group atoms respectively. It can be considered as a face-centered-cube lattice with a basis as marked by the arrow.

A Bravais lattice is an infinite array of discrete points with an arrangement and orientation appearing exactly the same from whichever point the array is viewed. That is to say, any point in the lattice can be expressed by:

$$\mathbf{R} = n_1\mathbf{a}_1 + n_2\mathbf{a}_2 + n_3\mathbf{a}_3 \tag{1.1}$$

where $\mathbf{a}_1$, $\mathbf{a}_2$ and $\mathbf{a}_3$ are called primitive vectors; n_1, n_2 and n_3 are integral number representing the position of the point with respect to the origin.

Figure 1.3 (a) shows a set of primitive vectors for the FCC lattice. Note that the set of primitive vectors is not unique; in fact there are infinite numbers of choices for any given Bravais lattice. This set of primitive vectors is a symmetric set compared to the x, y, and z-axes. A similar set of such vectors for the body-centered cubic (BCC) lattice is shown in Figure 1.3 (b). The reason we mention BCC lattice here is not only that it is a very important type of lattice in solids, but also it is the reciprocal lattice of the FCC lattice.

The reciprocal lattice is the Fourier transform of the original lattice, or so-called direct lattice. It can be presented by a set of points **K** in Fourier space satisfying the following condition:

$$e^{i\mathbf{K}\cdot\mathbf{R}} = 1 \tag{1.2}$$

for all **R** in the Bravais lattice. A equivalent definition is to express **K** as:

$$\mathbf{K} = k_1\mathbf{b}_1 + k_2\mathbf{b}_2 + k_3\mathbf{b}_3 \tag{1.3a}$$

$$\mathbf{b}_i \cdot \mathbf{a}_j = 2\pi\delta_{ij} \tag{1.3b}$$

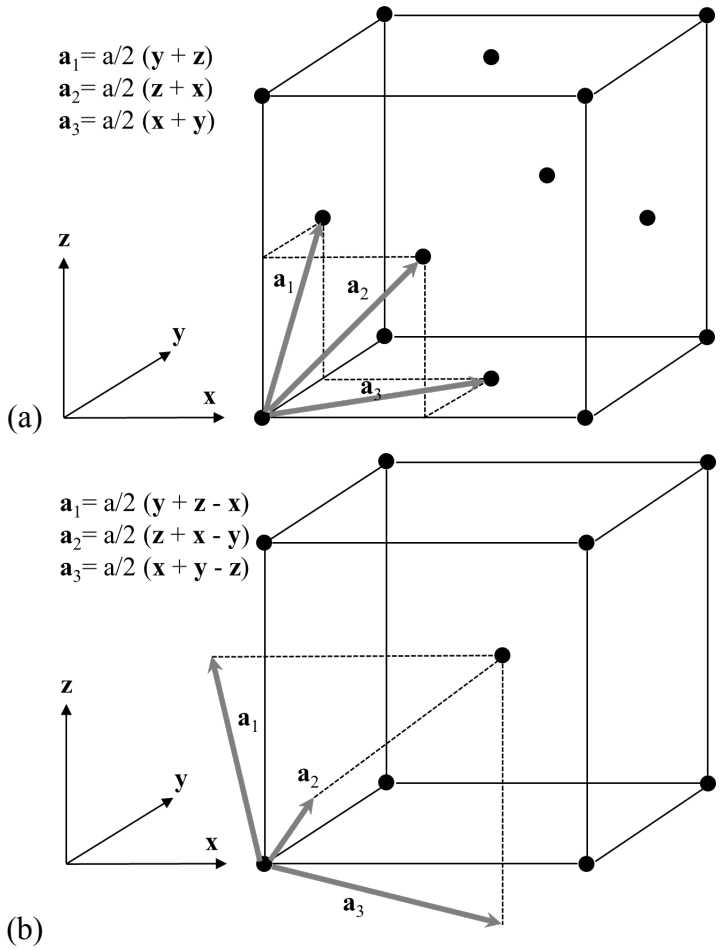

Figure 1.3: Sets of primitive vectors for the FCC (a) and BCC (b) lattice. The primitive vectors are expressed using three orthogonal unit cell vectors **x**, **y** and **z** as shown in the left.

By applying the primitive vectors of the FCC and BCC lattices in Figure 1.3 to equation (1.3b) and multiplying $4\pi/a^2$ to the left of the equation, one can prove that either lattice is the reciprocal lattice of the other.

It is apparent from equation (1.2) that for any vector **K** in reciprocal space, there will be a set of real space planes perpendicular to **K** that satisfies the equation. In another word, there is a correspondence between reciprocal lattice vectors and families of direct lattice planes. The Miller indices *h, k, l* are the coordinates of the shortest reciprocal lattice vector ($h\mathbf{b}_1 + k\mathbf{b}_2 + l\mathbf{b}_3$) normal to the set of direct lattice planes that intersect the axes at the points ($x_1\mathbf{a}_1$, $x_2\mathbf{a}_2$, $x_3\mathbf{a}_3$), where

$$h:k:l = \frac{1}{x_1}:\frac{1}{x_2}:\frac{1}{x_3} \tag{1.4}$$

and *h, k, l* are integers with no common factors. Note that the real space axes ($\mathbf{a}_1$, $\mathbf{a}_2$, $\mathbf{a}_3$) are normally the vectors for cubic, conventional (i.e. non-primitive) unit cells as shown in Figure 1.x. Crystallographers use (*h k l*) to denote these planes, and [*h k l*] to represent the direction perpendicular to those planes.

1.1.2 Electronic band structure

The first Brillouin zone is the region of space that is closer to one point than to any other point in the reciprocal lattice. Figure 1.4 (a) shows the first Brillouin zone of the BCC reciprocal lattice or the FCC direct lattice. The characteristic symmetry points are marked in the figure. A good starting point of understanding the band structure of semiconductors is the nearly free electron approximation. An example is shown in Figure 1.4 (b), which was constructed by plotting the value of the free electron energy $\varepsilon(\mathbf{k}) = \hbar^2(\mathbf{k} - \mathbf{G})^2/2m$, as vector **k** varied from one symmetry point to another (along the vector **G** which is the vector connecting symmetry points).

To calculate the real band structure, one has to explore the approximate solutions to the Schrödinger equation (assuming every electron experience the same potential ***V***, i.e. one-electron Schrödinger equation):

$$\boldsymbol{H}\psi_n(\boldsymbol{r}) = \left(\frac{\boldsymbol{p}^2}{2m} + V(\boldsymbol{r})\right)\psi_n(\mathbf{r}) = E_n\psi_n(\boldsymbol{r}) \tag{1.5}$$

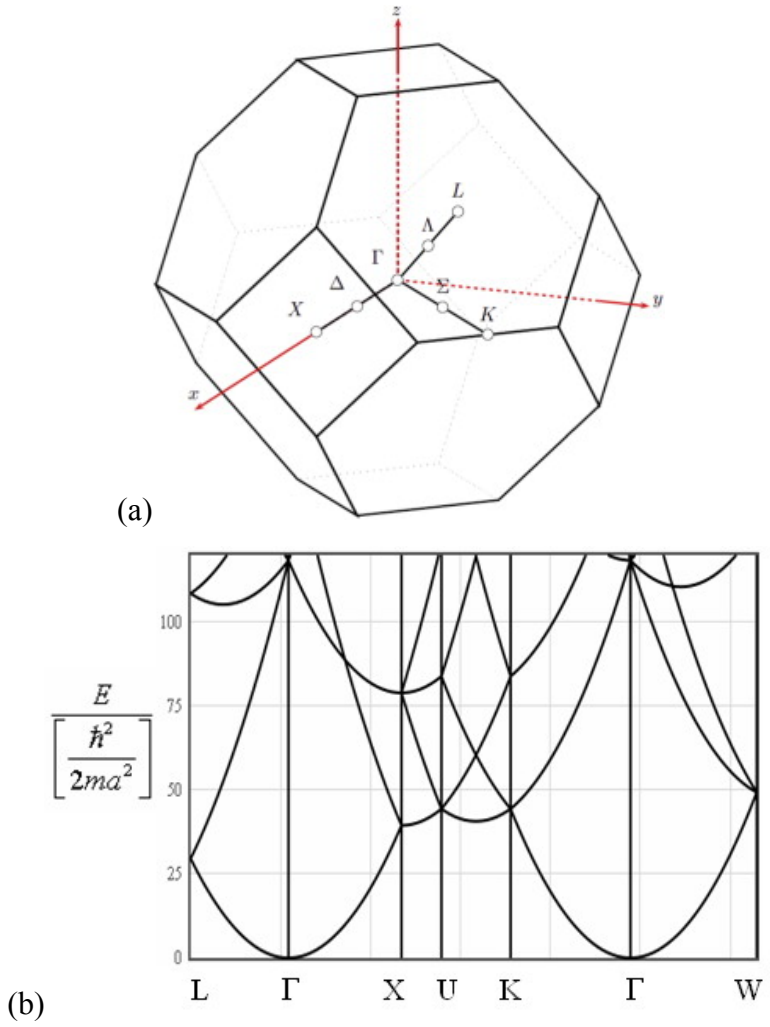

Figure 1.4: (a) The first Brillouin zone of the FCC direct lattice. Some of the high-symmetry points are marked in the figure. (b) Free electron energy levels for an FCC lattice. [5] The energies are plotted along lines in the first Brillouin zone joining the points Γ, K, L, W, X.

where $\boldsymbol{H}$, $\psi_n(\boldsymbol{r})$ and E_n denote the one-electron Hamiltonian, the wavefunction and energy of an electron in an eigenstate labeled by n; $\boldsymbol{r}$ is the position vector. Analytical solutions are often obtained in two opposite limits of the particle energy E with respect to the potential V. One is to assume that the potential is weak enough so the band structure can be treated by adding a weak potential perturbation to the nearly free electron calculations, such as the pseudopotential method [6]. The methods of this type aim at nearly free electrons such as those in conduction bands,

while the more localized valence band electrons (like bonding orbitals) can be described by the opposite limited, the so-called tight-binding approximation. It assumes that the electrons have relatively small energy and are tightly bound to their nuclei. In this case, the overlap of atomic wave functions or orbitals between two adjacent atoms is small but enough to require correction to the case of isolated atoms. So the band structure can be defined by a set of overlap parameters between atomic orbitals. An empirical tight-binding model can be found in Ref. [7].

The most economical description of the energy bands in semiconductors is the effective mass approximation, also known as the envelope function approximation or the multiband $\boldsymbol{k}\cdot\boldsymbol{p}$ method. Unlike the pseudopotential or tight-binding method, the input parameters of the $\boldsymbol{k}\cdot\boldsymbol{p}$ method are energy gaps and optical matrix elements which are less in number and can be determined experimentally. Using the Bloch wavefunction, the one-electron Schrödinger equation (1.5) can be expressed in the following form:

$$\left(\frac{p^2}{2m}+\frac{\hbar\boldsymbol{k}\cdot\boldsymbol{p}}{m}+\frac{\hbar^2k^2}{2m}+V\right)u_{nk}=E_{nk}u_{nk} \tag{1.6a}$$

$$\psi_{nk}(\boldsymbol{r})=\exp(i\boldsymbol{k}\cdot\boldsymbol{r})u_{nk}(\boldsymbol{r}) \tag{1.6b}$$

where n is the band index, u_{nk} has the periodicity of the lattice. Using the perturbation theory in the second order, the eigenvalues E_{nk} can be obtained (here in the nondegenerate case for simplicity):

$$E_{nk}=E_{n0}+\frac{\hbar^2k^2}{2m}+\frac{\hbar^2}{m^2}\sum_{n'\neq n}\frac{|\langle u_{n0}|\boldsymbol{k}\cdot\boldsymbol{p}|u_{n'0}\rangle|^2}{E_{n0}-E_{n'0}} \tag{1.7}$$

where the term $\langle u_{n0}|\boldsymbol{k}\cdot\boldsymbol{p}|u_{n'0}\rangle$ is the matrix element between electronic levels, e.g. conduction band and the hole bands.

Since most of the electronic and optical properties of semiconductors are determined by the comparatively small numbers of electrons excited into the conduction band (CB) near the conduction band minimum (CBM) and holes left behind in the valence band (VB) near the valence band maximum (VBM), the band edges are often approximated by a parameter called "effective mass", which is the second derivative of the parabolic function $E(\boldsymbol{k})$. The $\boldsymbol{k}\cdot\boldsymbol{p}$ method

allows to derive analytical expressions for the energy dispersion and the effective mass m^*, since equation (1.7) can be expressed as:

$$E_{nk} = E_{n0} + \frac{\hbar^2 k^2}{2m^*} \tag{1.8a}$$

$$\frac{1}{m^*} = \frac{1}{m} + \frac{2}{m^2 k^2} \sum_{n' \neq n} \frac{|\langle u_{n0} | \boldsymbol{k} \cdot \boldsymbol{p} | u_{n'0} \rangle|^2}{E_{n0} - E_{n'0}} \tag{1.8b}$$

Figure 1.5 shows the band structure of InAs calculated by an 8 level $\boldsymbol{k} \cdot \boldsymbol{p}$ model in Ref [8]. Generally there are four bands near the energy gap of III-V semiconductors: one conduction band and three valence bands, namely heavy hole, light hole and split-off bands. The terms "heavy" and "light" are based on the difference in effective masses.

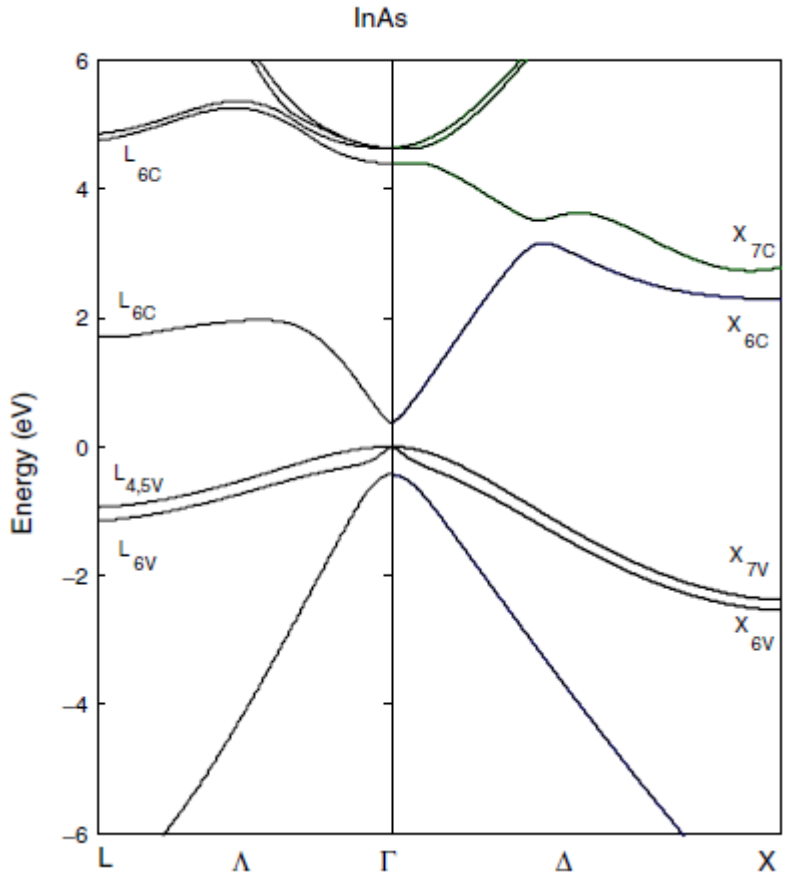

Figure 1.5 Energy bands of InAs calculated by a 30-band $\boldsymbol{k} \cdot \boldsymbol{p}$ Hamiltonian in the [111] and [110] directions of k space [8].

Many important properties of semiconductors are determined by effective mass, e.g., the density of states (DOS). It describes the number of available states per interval of energy at each energy level and can be calculated from the effective mass. DOS in CB in xxx in non-degenerate case can be calculated by:

$$N_c(T) = \frac{1}{4}\left(\frac{2m_c^* k_B T}{\pi\hbar^2}\right)^{3/2} \tag{1.9}$$

where m_c^* is the DOS effective mass in CB, k_B is the Boltzmann constant, T is the lattice temperature.

1.1.3 Parameters for III-V alloys

Heterojunctions are widely used in most semiconductor devices. This requires the growth of different semiconductor materials on the same substrate. Device heterostructures are preferably grown on binary substrates because of their high crystalline quality. GaSb is often the choice of substrates for mid- to long-wave infrared devices for the following reasons. (a) Devices with certain thickness (more than a few hundred nm) have to be grown on lattice matched substrate to minimize dislocations that deteriorate device performance. GaSb has a lattice constant of ~ 6.1 Å and there are many lattice matched alloys to form device heterostructures; AlAsSb, AlGaAsSb, and GaInAsSb to name a few. In the opposite case, InSb has a lattice constant of ~ 6.5 Å and there are no other lattice matched semiconductors. (b) Figure 1.6 plots the energy positions of the CBM and VBM of III-V binaries. Unlike InAs which has the lowest valence band offset (VBO), GaSb has a moderate VBO so lattice matched alloys can form barriers for either electrons or holes. It provides flexibility in the design of various heterostructures.

Conventional III-V alloys lattice matched to GaSb include AlAsSb, InAsSb, AlGaAsSb, GaInAsSb, and quinary alloy AlGaInAsSb. Figure 1.7 shows the band gap energy versus lattice constant plot for III-V binary and ternary alloys containing III-group elements Aluminum, Gallium, Indium and V-group elements Arsenic, Antimony. The lattice constant of alloys is calculated using linear interpolation. The band gap energy is calculated assuming a bowing parameter C defined as following:

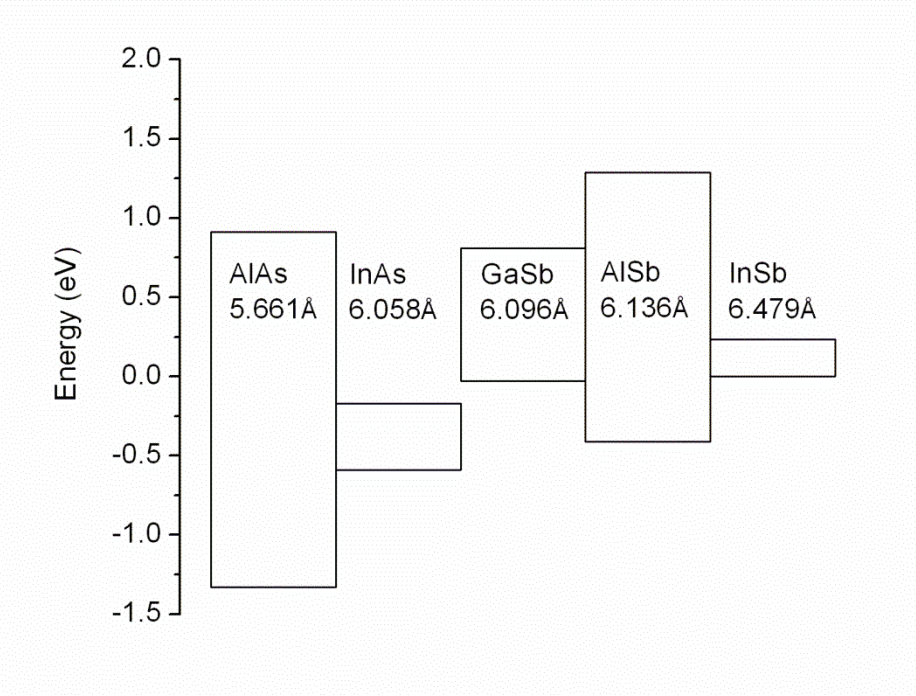

Figure 1.6: Band alignment of the CBM and VBM for binaries AlAs, InAs, GaSb, AlSb and InSb [1]. The top edge and bottom edge of each box correspond to CBM and VBM respectively. The band alignment between AlAs and InAs (or GaSb and AlSb) is type I alignment while that between InAs and GaSb is type II broken gap alignment.

$$E_g(A_{1-x}B_x) = (1-x)E_g(A) + xE_g(B) - x(1-x)C \tag{1.10}$$

where C accounts for the deviation from linear interpolation between two binaries A and B. The values of the bowing parameter in most alloys are determined empirically and the nature of this effect is beyond the scope of this work.

The effective mass of alloys can be determined from those of the binaries under the framework of Kane using $\boldsymbol{k \cdot p}$ method with the following Kane parameter F [9]:

$$F = \frac{1}{m}\sum_r \frac{\left|\langle S|p_x|u_r\rangle\right|}{(E_c - E_r)} \tag{1.11}$$

where the term in the bra-ket is the matrix element between the s-like conduction band and the p-like valence band, similar to that in equation (1.7). One can interpolate the F linearly to obtain the effective mass of alloys.

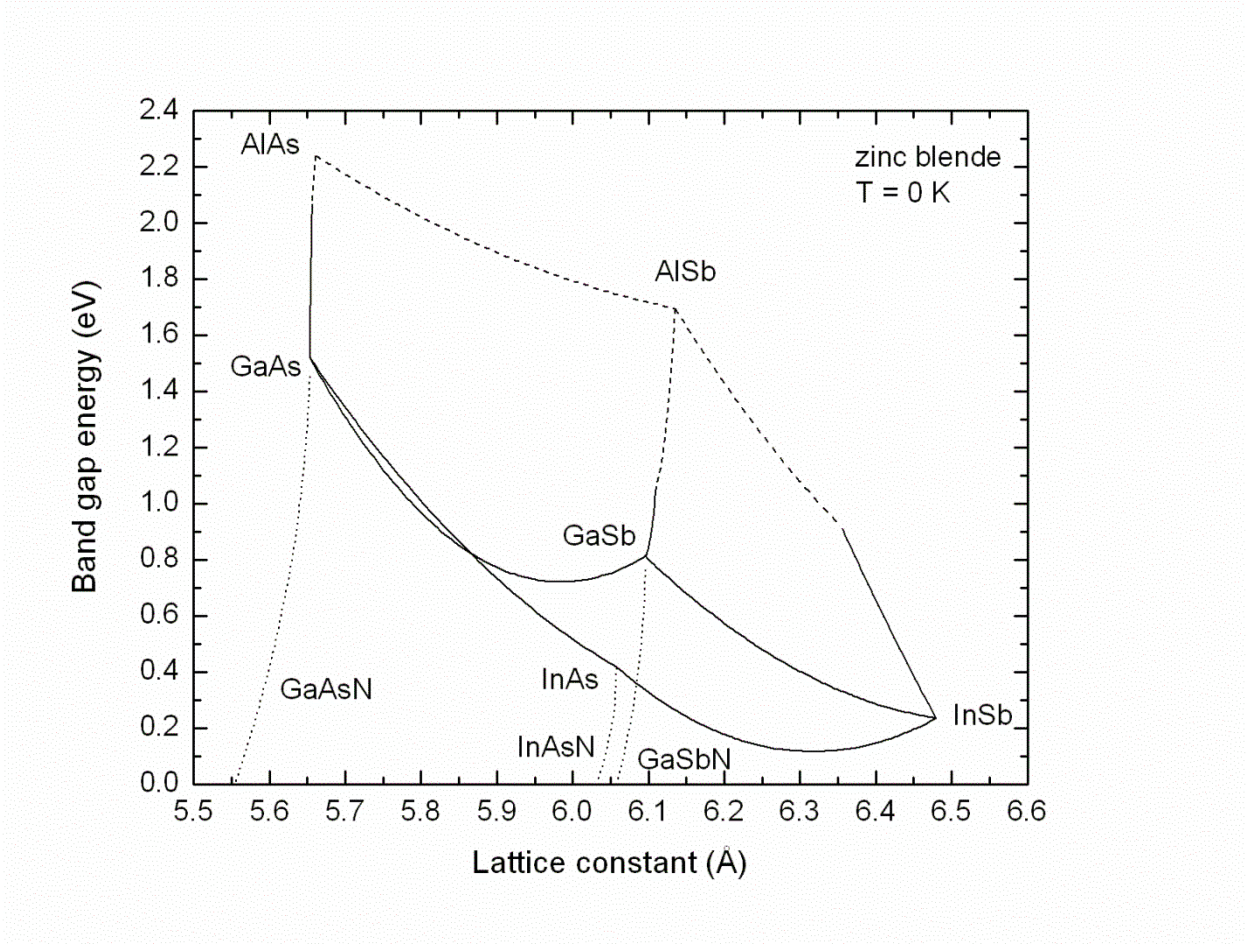

Figure 1.7: Band gap energy as a function of lattice constant for the zinc blende binary and ternary arsenides and antimonides. The bowing parameters are taken from [1] except for InAsSb, in which the bowing parameter of 0.8 eV is used according to [10]. The solid lines are direct Γ-valley band gaps and the dashed lines are indirect X-valley band gaps. The dotted lines schematically show the band gaps versus lattice constant for dilute nitrides.

The methodology discussed above is not suitable for dilute nitride materials, in which a few percent of nitrogen atoms drastically changes the electronic and optical properties of the "host" III-V alloys. A more comprehensive introduction of dilute nitride materials will be presented in Chapter 2.

Apart from the "bulk" semiconductors in which electrons are free to move in three dimensions, quantized electronic structures can confine the electrons in two or one dimensions, modify the bulk DOS, effective mass and etc., and are often used in semiconductor lasers, LEDs and detectors, as will be discussed next.

1.2 III-V optoelectronic devices in the middle and long wavelength infrared regions

In this section we will go through some currently available MWIR and LWIR emitters and detectors. For the sake of the aim of this work, we will focus on the aspects of heterostructure design and material system.

1.2.1 Lasers

There are generally three types of lasers working in this wavelength range: type I quantum well (QW) lasers, quantum cascade lasers (QCLs) and interband cascade lasers (ICLs). GaSb-based type I lasers normally utilize (Al)GaInAsSb alloys as the waveguide core and wider band gap, lower refractive index AlGaAsSb alloys as the cladding layers to form double heterostructures. QWs are made of GaInAsSb alloys with higher Indium and less Arsenic composition to form barriers and confine electrons and holes. Compressively strained QWs are employed to reduce the DOS of holes and to help improve the hole confinement. This type of lasers works in a wavelength range typically from 2–3.5 μm with sub-watt to watt level continuous wave (cw) output power in room temperature [11,12]. Operation in longer wavelengths is limited by the fundamental band gap of QW material and the quantization energies.

Compared to type I lasers, QCLs are unipolar; electrons are recycled, re-injected into an adjacent active region after emitting photons. The laser emission is achieved by the intersubband transition of electrons, which is a much faster process (~ps) than the interband transition between electrons and holes (~ns). To reach population inversion, electrons in the ground level are rapidly (~0.1 ps) removed by phonon-electron scattering. The energy levels in QCLs do not exist naturally in the constituent materials but are artificially created by QW using the CB offset between consecutive layers. The InGaAs/AlAsSb material system lattice matched to InP substrates has a CB offset of ~ 1.6 eV and is commonly used for the fabrication of QCLs. High

power (watt level) room temperature cw operating QLCs have been demonstrated with emission wavelengths covering the MWIR and LWIR region [13, 14, 15].

In contrast to QCL, the cascade scheme in ICLs is done by a semimetallic interface using the type II alignment between GaSb and InAs. The CBM in InAs is ~ 0.2 eV below the VBM of GaSb so the electrons and holes can be generated internally with an applied bias. The active region is formed by a GaInSb hole QW sandwiched between two InAs electron QWs. The emission wavelength can be tuned by changing the quantization energy in electron QWs. Cw operation of ICLs at room temperature has been demonstrated with emission wavelengths from about 3–6 μm [3]. Those ICLs are grown on GaSb substrate; the materials used in the structure include InAs, Ga(In)Sb and AlSb.

1.2.2 Light emitting diodes

In general LEDs can be fabricated by p-i-n junctions where electrons and holes are injected to the intrinsic active region and recombine to emit photons, like lasers but without optical resonators. In fact all the aforementioned laser designs in this wavelength region have been adopted to create LEDs, e.g. type I QW LEDs [16], quantum cascade LEDs [17] and interband cascade LEDs [18]. Since LED emits light mostly by spontaneous emission, it does not require population inversion; the carrier density in the active region is much less than in lasers. For this reason bulk type active region, which would suffer from Auger recombination in case of laser, can be utilized in LEDs. Similarly, InAs/GaSb SL was also used as the active region in MWIR and LWIR LEDs [19, 20].

1.2.3 Photodetectors

Photodetectors are devices that absorb photons and separate photo-excited carriers to generate voltage or current. Conventional types include p-i-n photodiodes and photoconductive detectors; both apply an electrical field to the light-absorbing region to separate photo-excited carriers. However for MWIR and LWIR detectors when an electrical field is applied to the narrow gap absorbing region, tunneling and other sources of dark current generates high noise and deteriorates device performance. Barrier type photodetector designs were recently developed to solve this problem [21, 22, 23, 24, 25, 26] as will be discussed in details in Chapter 4. This type of detectors usually utilizes SL materials including InAs/GaSb SL [23, 24, 26],

InAs/InAsSb SL [25] in the device heterostructure; background limited performance has been achieved at elevated temperatures (~120 K) from 5 μm to 12 μm.

Chapter 2 Characterization of dilute nitride materials

"Dilute" nitride is a type of alloy in which a few percent of anion atoms in the conventional III-V "host" semiconductor is substituted by nitrogen. A strong reduction of band gap associated with nitrogen incorporation has been observed in several dilute nitride materials such as GaAsN, InAsN, GaInAsN, GaSbN, GaAsSbN, InPN, and InSbN [27, 28, 29, 30, 31, 32, 33]. Due to the small covalent radius and high electronegativity, nitrogen atoms strongly modify the band structure of conventional III-V alloys, rendering interesting physical phenomena.

The band structure of dilute nitride has been studied using several approaches [34, 35]. In many cases, like in GaAsN, the observed band gap reduction can be roughly described by a simple band anticrossing (BAC) model [29]. It assumes that nitrogen induces a localized resonant state above the conduction band edge of the host material. Due to the anticrossing nature of the two electronic bands, the interaction pushes down the conduction band edge and causes the reduction of band gap. However, this idealized case where a single nitrogen atom replaces an anion atom is not suitable for many dilute nitrides, because the mismatch in the atom size between nitrogen and large V-atoms (e.g. antimony) often leads to a significant fraction of nitrogen atoms being incorporated into non-substitutional sites [36, 37].

Our work was focused on the characterization of GaSbN and InAsN materials. We demonstrated the reduction of optical band gaps with increasing nitrogen concentration and characterized the excess carrier lifetimes. For GaSbN, a bandgap reduction by up to 300 meV was observed in a sample with 1.4% of nitrogen; room temperature carrier relaxation times in the picosecond range were measured. For InAsN, the measured bandgap reduction was up to 150 meV in a sample with 2.25% of nitrogen; carrier lifetimes in the nanosecond range were measured.

2.1 Properties of GaSbN

A strong reduction of the fundamental bandgap with increased nitrogen content has been previously predicted for GaSbN alloys [30]. A theoretical tight-binding analysis of how nitrogen incorporation affects the material bandgap revealed a strong sensitivity to N complexes, [35] implying a restricted applicability of the widely used band anticrossing model (BAC) [29]. While a red shift of the absorption edge with increased nitrogen content was observed for GaSbN

grown on lattice mismatched GaAs substrates (corresponding to a tensile strain above 7%) [38, 39], it was not apparent which optical transitions (*i.e.*, direct or indirect; allowed or forbidden) accounted for the observed spectra. No reports on the corresponding photoluminescence (PL) from GaSbN bulk materials have been published so far. The observed PL from dilute-nitride-antimonide quantum-well (QW) samples [40, 41] is more complicated to interpret with regard to the fundamental material bandgap.

This section will present the results of a comprehensive absorption and photoluminescence study of GaSbN bulk materials grown on nearly-lattice-matched GaSb substrates. The data reveal the effect of nitrogen incorporation on the fundamental bandgap, and on the character of band edge optical transitions in dilute-nitride GaSbN bulk materials.

The dilute-nitride alloys were grown by solid-source molecular beam epitaxy on nominally-undoped GaSb substrates (residual *p*-type doping level $\approx 10^{17}$cm^{-3} at room temperature). Nitrogen was introduced into the growth chamber using an rf plasma gas source. The nitrogen compositions were determined from high-resolution X-ray rocking curves to vary from 0.3 to 1.4%. Since the lattice mismatch between the substrate and the GaSbN epitaxial layers corresponds to a tensile strain below 0.4%, little (if any) strain relaxation is expected.

Two groups of samples were grown and characterized. One group (A) was designed for absorption studies. These samples comprised a 2-μm-thick GaN_xSb_{1-x} layer grown directly onto a GaSb buffer. The other group (B) was designed for PL and Hall analysis. These samples comprised a 1-μm-thick GaN_xSb_{1-x} layer sandwiched between Al-containing wide bandgap materials to assure confinement of the carriers and electrical isolation from the substrate. A thin GaSb cap was grown on top to prevent rapid oxidation of the AlAsSb in atmosphere.

Figure 2.1 shows temperature-dependent Hall densities and mobilities acquired at a magnetic field of 1 Tesla for two samples from Group B with nitrogen concentrations of 0.6% (solid circles) and 1.2% (open squares). The AlAsSb barriers in these samples electrically isolate the GaSbN epi-layers from the conducting GaSb substrates. Both samples are found to be *p*-type, with concentrations ranging from 7-9 $\times 10^{18}$ cm^{-3} at 300 K to as little as 7×10^{15} cm^{-3} for the 0.6% sample at 4.5 K. The nature of the gradual freeze-out of the hole population is not understood. The inset to Figure 2.1 plots corresponding dependences of the hole mobilities on temperature. From ≈ 50 cm^2/Vs at 300 K, the hole mobility in the 0.6% sample increases to 1300 cm^2/Vs at $T = 4.5$ K.

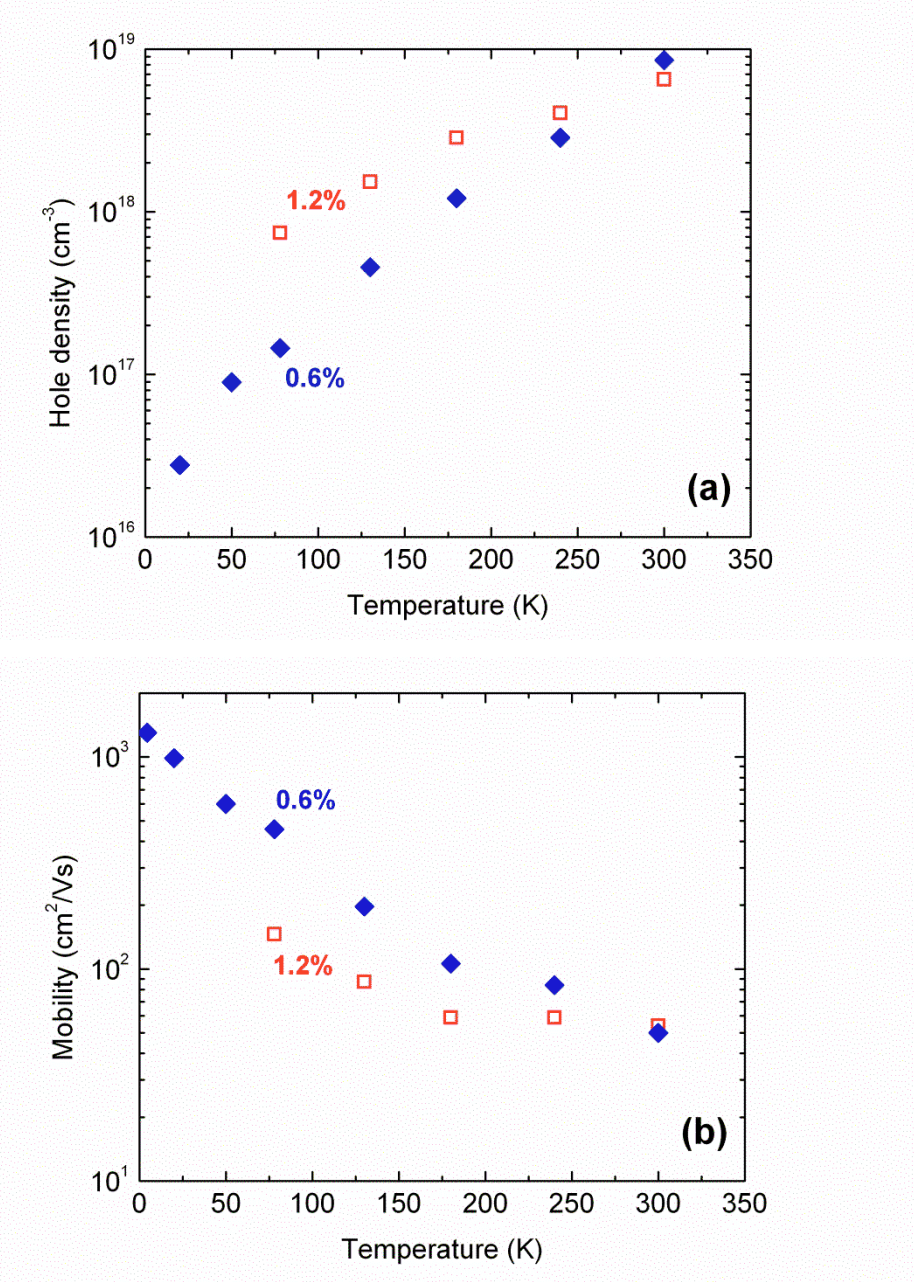

Figure 2.1: Hole concentrations (a) and mobilities (b) versus temperature for group B samples with 0.6% (blue solid diamonds) and 1.2% (red open squares) nitrogen, from Hall measurements at 1 T. Data for the 1.2% sample became unreliable at the lowest temperatures.

Optical absorption spectra were determined from transmission measurements made using a Fourier transform infrared (FTIR) spectrometer equipped with liquid nitrogen cooled InSb and MCT detectors. The transmission spectra were analyzed assuming multiple reflections in the

sample and the absence of fringes [42]. Transmission measurements were performed for both the grown samples and their substrates. With residual hole concentrations of order 10^{17} cm^{-3}, the GaSb substrates exhibited free carrier absorption coefficients of ≈ 40 cm^{-1} at 0.3 eV, which is similar to previous reports [42]. The substrate absorption spectra were subtracted from those of the samples to isolate the epi-layer band-to-band absorption from the free carrier absorption. The resulting absorption spectra $\alpha(h\upsilon)$ obtained for samples with nitrogen compositions of 0.3, 0.7 and 1.4% are presented in Figure 2.2 (a).

At photon energies approaching the room-temperature GaSb bandgap of ≈ 0.72 eV, the extracted experimental transmission spectra become distorted by strong absorption in the thick substrates. Note also that the spectrum for the sample with 0.3% nitrogen shows some Fabry-Perot fringing. This sample belongs to group B, for which the AlAsSb carrier confinement layers surrounding the GaSbN provide a large refractive-index contrast. On the other hand, the two samples from group A (0.7% and 1.4% of nitrogen) display no significant fringing. The GaSbN absorption edge is seen to experience a significant red shift with increasing nitrogen content, in agreement with previously published data [38, 39]. Figure 2.2 (b) shows the same GaSbN spectra plotted in coordinates of $(\alpha \cdot h\upsilon)^2$ versus $h\upsilon$, for which direct allowed optical transitions between parabolic bands should appear as straight lines (see for instance [43]). Near the band edge, experimental absorption edges typically fit the expression $\alpha \sim (h\upsilon - E_g)^{1/2}/h\upsilon$. The increased absorption in the $GaN_{0.014}Sb_{0.986}$ sample at energies above 0.55eV can be attributed to the strong conduction band nonparabolicity expected in dilute-nitrides. The fit of the sample with 0.3% of nitrogen is less satisfactory, presumably due to the observed spectral fringing and its close proximity to the GaSb edge.

The fundamental bandgap (E_g) can be estimated from the intercept, as shown in Figure 2.2 (b). A bandgap reduction of about 300meV compared to GaSb is observed in the 1.4% nitrogen sample. The large absorption coefficient approaching 10^4 cm^{-1} and the absorption edge's functional dependence on energy imply that this GaSbN material indeed has a direct bandgap as predicted by theoretical calculations [30, 35]. The absorption spectra of the samples with 0.7% and 1.4% nitrogen were also measured at 15K (Figure 2.2 (c)). As expected, the GaSbN bandgap increases with decreasing temperature, although the observed effect becomes less pronounced at higher nitrogen content (~85 meV for GaSb [1], ~60 meV for $GaN_{0.007}Sb_{0.993}$, and only ~30 meV

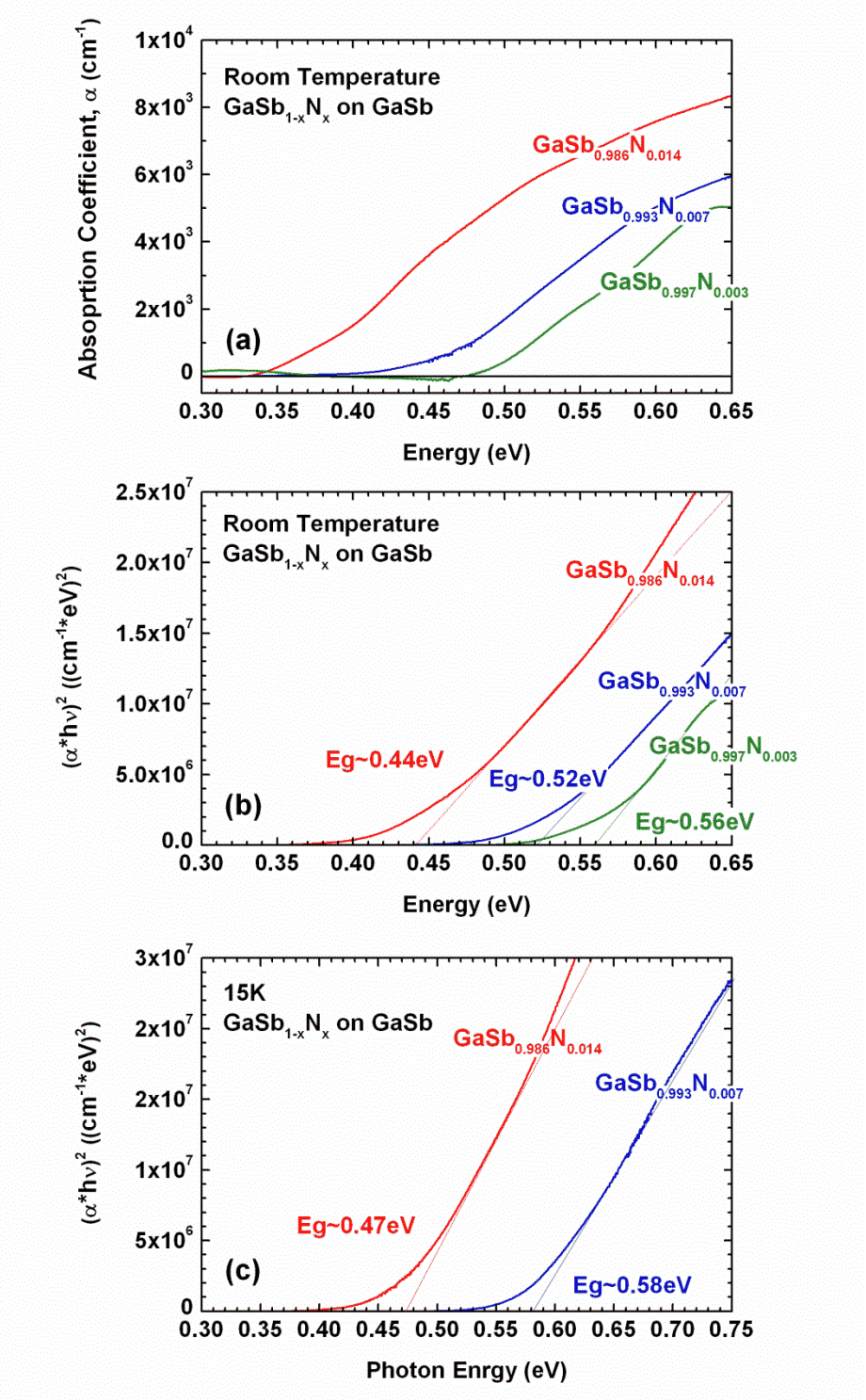

Figure 2.2: (a) Absorption spectra at room temperature for three GaSbN layers with 0.3%(green), 0.7% (blue) and 1.4% (red) of nitrogen; (b) room temperature absorption spectra plotted in coordinates corresponding to direct allowed optical transitions; (c) absorption spectra at 15 K.

for $GaN_{0.014}Sb_{0.986}$), the direction predicted by theory [44]. For a hole density of 10^{19} cm^{-3}, the Moss-Burstein shift at room temperature is estimated to be ≈35 meV, assuming the valence band of GaSbN is similar to that of GaSb. This implies that the actual energy gap is smaller than the value indicated in Fig. 2.2 by that amount. At low temperatures, the carrier freeze-out leads to a negligible shift of the absorption edge.

We applied the ultra-fast up-conversion-technique to study PL in GaSbN bulk materials [45]. In this experiment the light from a Nd:glass mode-locked 200fs/80MHz laser was divided into two beams, with one beam for excitation and the other for up-conversion. Mid-IR PL excited by the excitation pulse (20 mW average power focused down to 10^{-6} cm^2 on the sample) was mixed with the delayed up-conversion pulse in a nonlinear crystal (periodically poled Lithium Niobate). The sum frequency radiation was then dispersed by a spectrometer and registered by a GaAs-cathode photomultiplier tube. The setup is capable of detecting PL from materials with very short carrier lifetimes (the system temporal resolution is about 0.5 ps as estimated from autocorrelation measurements). Periodically poled Lithium Niobate crystals with different poling periods allowed for the effective up-conversion of mid-IR PL to cover the spectral range from below 2 μm to above 4 μm. The up-conversion photon energies were selected by choosing the crystal period and spectrometer grating position. The photoexcited carrier concentration necessary to observe the PL signal at room temperature was rather high, in the range 1-5 × 10^{18} cm^{-3}.

Figure 2.3 (a) shows the PL decay measured at different photon energies for the sample with 0.3% nitrogen. Immediately after the excitation pulse, the maximum PL signal occurs near 0.53eV (whereas no PL signal could be registered in this spectral region for the reference sample that contained a GaSb layer in place of the GaSbN). This PL peak energy agrees with the band gap energy estimated from the absorption studies (0.56 eV). Figures 2.3 (b) and (c) show the PL decays obtained for the two samples from group B with 0.6% and 1.2% nitrogen. Again, the peak energies of the initial PL signals are consistent with the fundamental bandgaps estimated for the group A samples with similar nitrogen contents, *i.e.*, near 0.5 eV and 0.41 eV. The presence of band-to-band photoluminescence again confirms the direct allowed nature of the optical transitions in dilute-nitride GaSbN bulk materials containing up to at least 1.4% nitrogen.

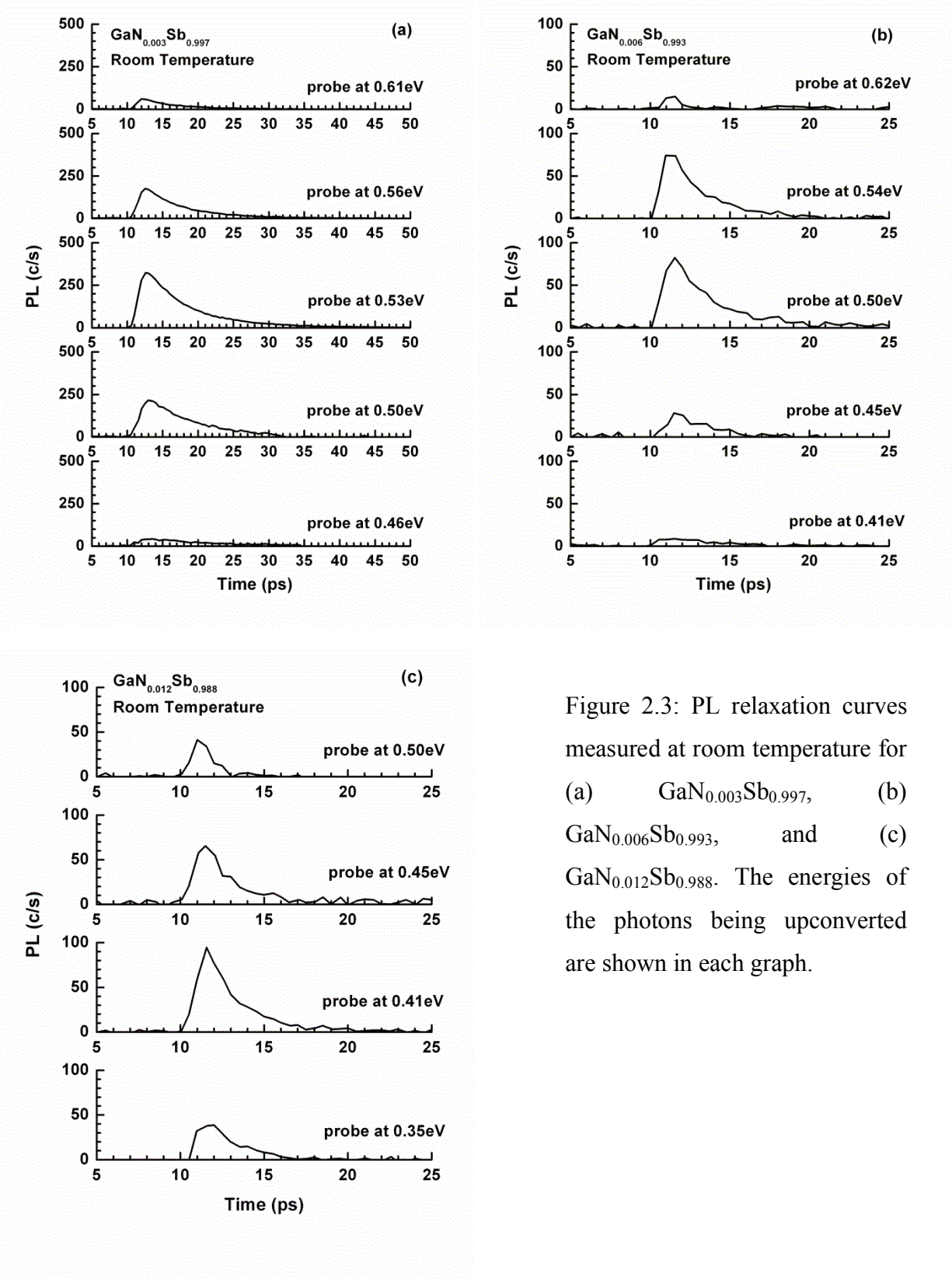

Figure 2.3: PL relaxation curves measured at room temperature for (a) $GaN_{0.003}Sb_{0.997}$, (b) $GaN_{0.006}Sb_{0.993}$, and (c) $GaN_{0.012}Sb_{0.988}$. The energies of the photons being upconverted are shown in each graph.

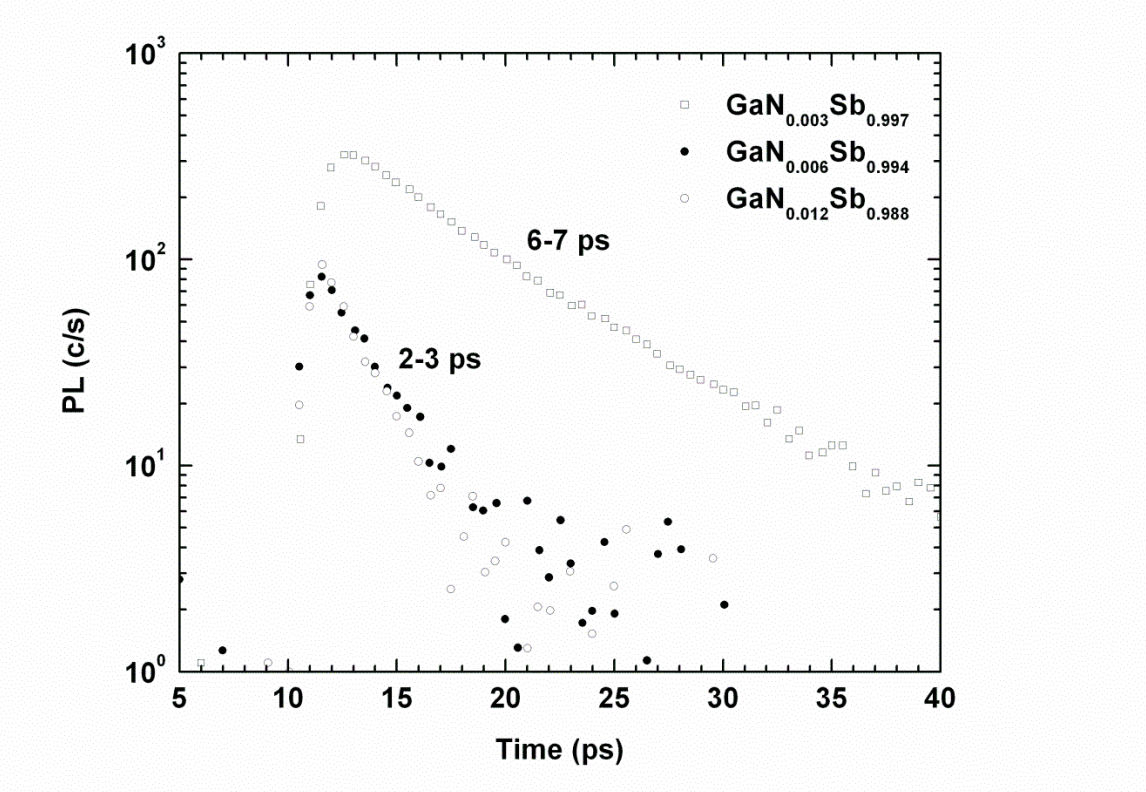

Figure 2.4: PL relaxation curves measured at room temperature for photon energies corresponding to maximum initial PL signal for GaSbN bulk materials with 0.3% (0.53 eV), 0.6% (0.5 eV), and 1.2% (0.41 eV) of nitrogen.

Figure 2.4 shows the PL temporal relaxation curves measured for the 0.3%, 0.6% and 1.2% nitrogen samples at photon energies corresponding to the initial PL maximum. Assuming linear recombination, the estimated carrier lifetimes are ≈ 6-7 ps for $GaN_{0.003}Sb_{0.997}$ and 2-3 ps for $GaN_{0.006}Sb_{0.993}$ and $GaN_{0.012}Sb_{0.988}$. The latter two samples exhibited less intensive initial PL signals, since their carrier relaxations competed with the PL rise times (note that in Figure 4, the PL signal for the 0.3% sample is still growing at a point where it is already starting to decay for the other two). The relaxation curves seem to be well fit by a single time constant despite the high excitation intensity (> 10^{18} cm^{-3}), which may be associated with the large residual doping levels. The rapid carrier relaxation dynamics are probably associated with recombination through defect states in the forbidden gap.

Summarizing, GaSbN bulk materials were grown by MBE with nitrogen contents of up to 1.4%. Hall measurements indicate residual hole concentrations of nearly 10^{19} cm^{-3} at room

temperature, but gradual freeze-out to below 10^{16} cm^{-3} (with hole mobility 1300 cm^2/Vs) in the 0.6% nitrogen sample at 4.5 K. Transmission experiments show that the absorption edge energy decreases by nearly 300 meV compared to GaSb for the sample with 1.4% nitrogen. The energies of the radiative transitions correlate well with the bandgap energies estimated assuming direct allowed band-to-band optical transitions. The carrier lifetimes determined from a nonlinear up-conversion technique, and assuming linear recombination, decrease from 6-7 ps to 2-3 ps when the nitrogen content is increased from 0.3% to 1.4%. Further studies are required to identify the physical mechanism responsible for the fast carrier relaxation dynamics in dilute-nitride GaSbN bulk materials.

2.2 Properties of InAsN

The strong band gap reduction in dilute nitrides can be utilized to extend the absorption range of the antimonide and arsenide binaries into the technologically important mid- and long-infrared region of the optical spectrum [30,46,47]. The rate of nonequilibrium carrier recombination is an important parameter for photonic materials. For instance, short minority carrier lifetime can limit the photodetector sensitivity [48]. High levels of residual carrier concentrations are often observed in dilute-nitride semiconductors. This is often interpreted as a consequence of crystalline imperfection possibly caused by technological constraints. Clearly, presence of defects can promote Shockley-Reed-Hall (SRH) recombination at high rates, rendering the material inadequate for high sensitivity photodetector applications. It was also predicted theoretically that nitrogen complexes can be formed in dilute-nitrides and create energy states in a bandgap [35]. The latter could be a fundamental reason for certain dilute-nitride alloys having short minority carrier lifetimes.

In the previous section we demonstrated GaSbN alloys had very short carrier recombination lifetimes on the order of several picoseconds. This observation was in qualitative agreement with theoretical predictions that GaSbN should have deep nitrogen complex levels in bandgap [35]. It is known that InGaAsN(Sb) dilute-nitrides are used as an active QWs material of 1.3-1.5 μm diode lasers of good quality [49,50]. It was predicted that in GaAsN, and especially in InSbN, the nitrogen complex states are in resonance or close enough to the conduction band and their role in determining the carrier lifetime should be reduced [35]. It is thus arguable that InAsN alloys can absorb light at wavelength above 5 μm while demonstrating

adequate SRH generation-recombination rates. Adding Sb to InAsN [51] can help to further reduce the material bandgap and ensure lattice matching to either InAs or GaSb substrates.

Growth of InAsN on InP substrates produced materials with residual electron concentration as high as about 10^{18} cm^{-3} for nitrogen composition of about 1 % [46]. The associated Moss-Burstein shift (about 100 meV per % of nitrogen) precluded the direct observation of the bandgap reduction in absorption spectroscopy experiments. In recognition of this observation later studies of the effect of nitrogen composition on bandgap of InAsN were performed solely by photoluminescence spectroscopy, see for instance [52]. Development of InAsN bulk material with room temperature photoluminescence at wavelength up to 4.5 μm was reported in year 2008 [53]. Optimized growth methodology improved the photoluminescence intensity and resulted into order of magnitude reduction of residual carrier concentration [54].

In this section we report on comprehensive photoluminescence and absorption spectroscopy studies of the dilute-nitride InAsN alloys with nitrogen composition up to about 2 %. The material was grown following the methodology reported in [52]. The ultra-fast photoluminescence up-conversion measurements were used to study the carrier relaxation dynamics.

The dilute-nitride alloys were grown by solid-source molecular beam epitaxy using a Veeco Uni-bulb rf plasma nitrogen source. Two sets of samples with different epi-layer thicknesses were grown on nominally undoped InAs substrate. The first set of six “thin” samples was developed to calibrate the rf nitrogen source and establish the growth methodology to control the N concentration. All samples were grown at a substrate temperature of 380 C. It is worth noting that no systematic growth optimization was done yet. The samples in this set comprised a 200-nm-thick InAsN layer grown directly onto an InAs buffer and capped with a ~ 20 nm InAs layer. Nitrogen incorporation was controlled by flux of N2 in RF plasma source, growth rate and temperature. High resolution x-ray diffraction was used to estimate the nitrogen composition, using Vegard’s law and assuming a lattice constant of cubic InN as 4.98 Å. Figure 2.5 shows the triple-axis rocking curves obtained for this sample with the lowest nitrogen content (0.65%) and with the highest one (2.25%). Pronounced pendellosung fringes demonstrate the flatness and general high crystalline quality of the films.

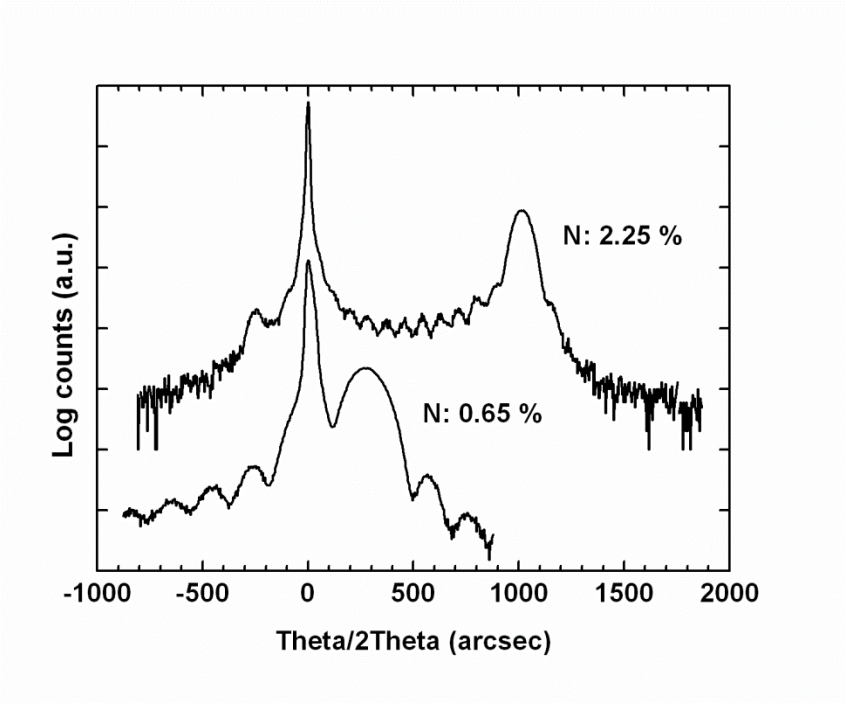

Figure 2.5: X-ray rocking curves for nitrogen 0.65% (bottom) and for 2.25% (top) for thin samples.

Following the system calibration two "thick" samples comprising 1.5-μm-thick InAsN layers with 1% and 2% of nitrogen were grown. The thick InAsN layers were sandwiched between 20 nm AlSb layers and a 20 nm InAs cap layer was grown on top to prevent rapid oxidation of AlSb in atmosphere. These layers obviously contain dislocations that resulted in a relaxation of 10-20% as estimated from the XRD reciprocal space mapping as shown in Figure 2.6 (a) and (b).

Temperature dependence of the equilibrium photoluminescence (PL) spectra was measured for a set of "thin" samples. Figure 2.7 (a) plots an exemplary set of curves obtained for the temperature near 20 K. The rightmost peak is PL from the InAs substrate with fundamental peak near 0.415 eV [55]. The PL from InAsN layer is red shifted. The amount of red shift is roughly proportional to the nitrogen content as determined from x-ray analysis. The InAsN PL peak clearly shows fine structure that was previously interpreted as combination of band-to-band (short wavelength) and bound-to-band (long wavelength) PL transitions [52]. The energy separation of these PL peaks is about 15 meV. Figure 2.7 (b) plots the nitrogen composition dependence of the energy of the short and long wavelength PL peaks. The dependence can be

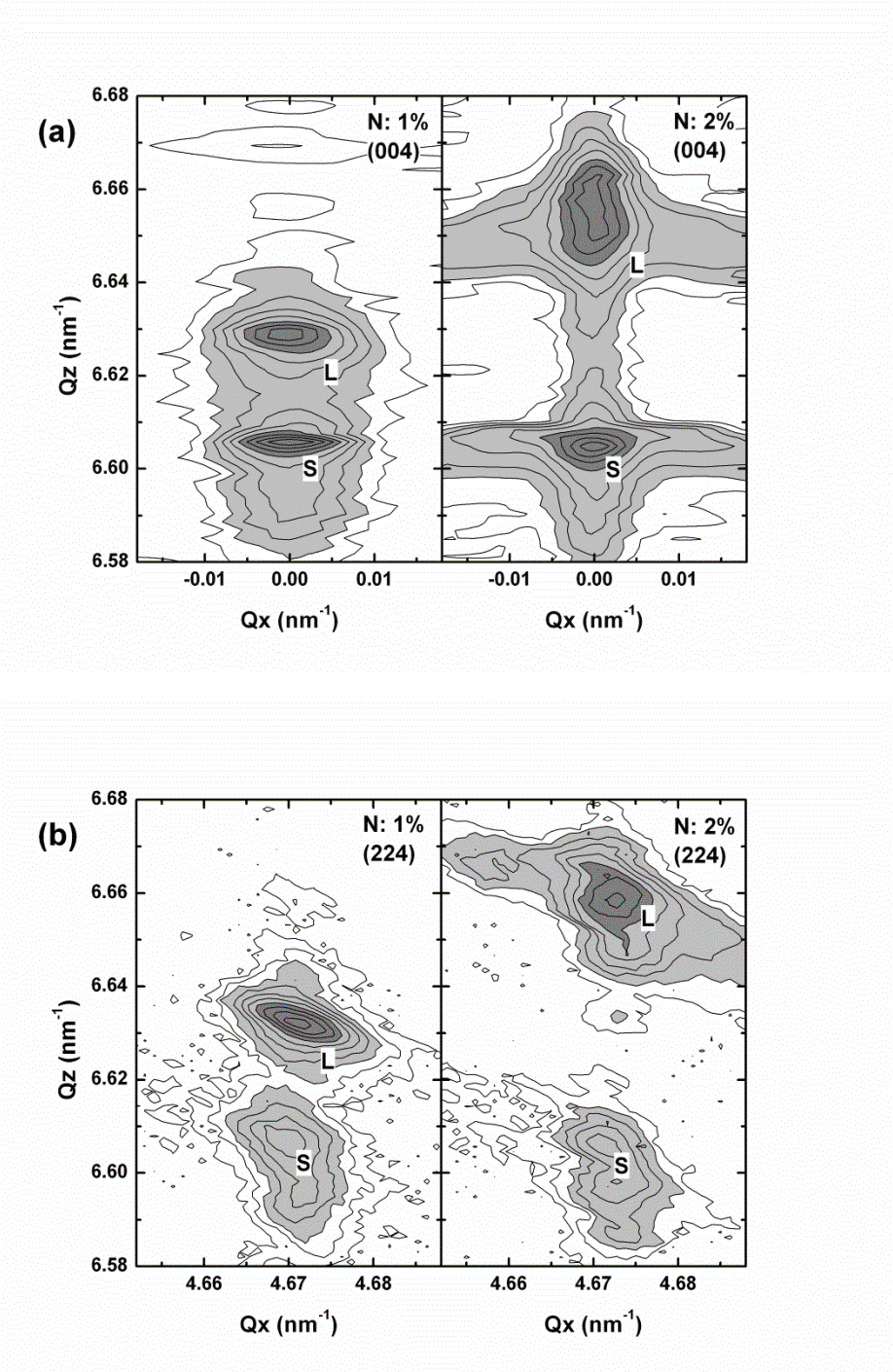

Figure 2.6: (a) 004 and (b) 224 reciprocal space scans for 1.5-mm-thick InAsN layer with 1% and 2% of nitrogen. Peaks S and L correspond to the substrate and the InAsN layer, respectively.

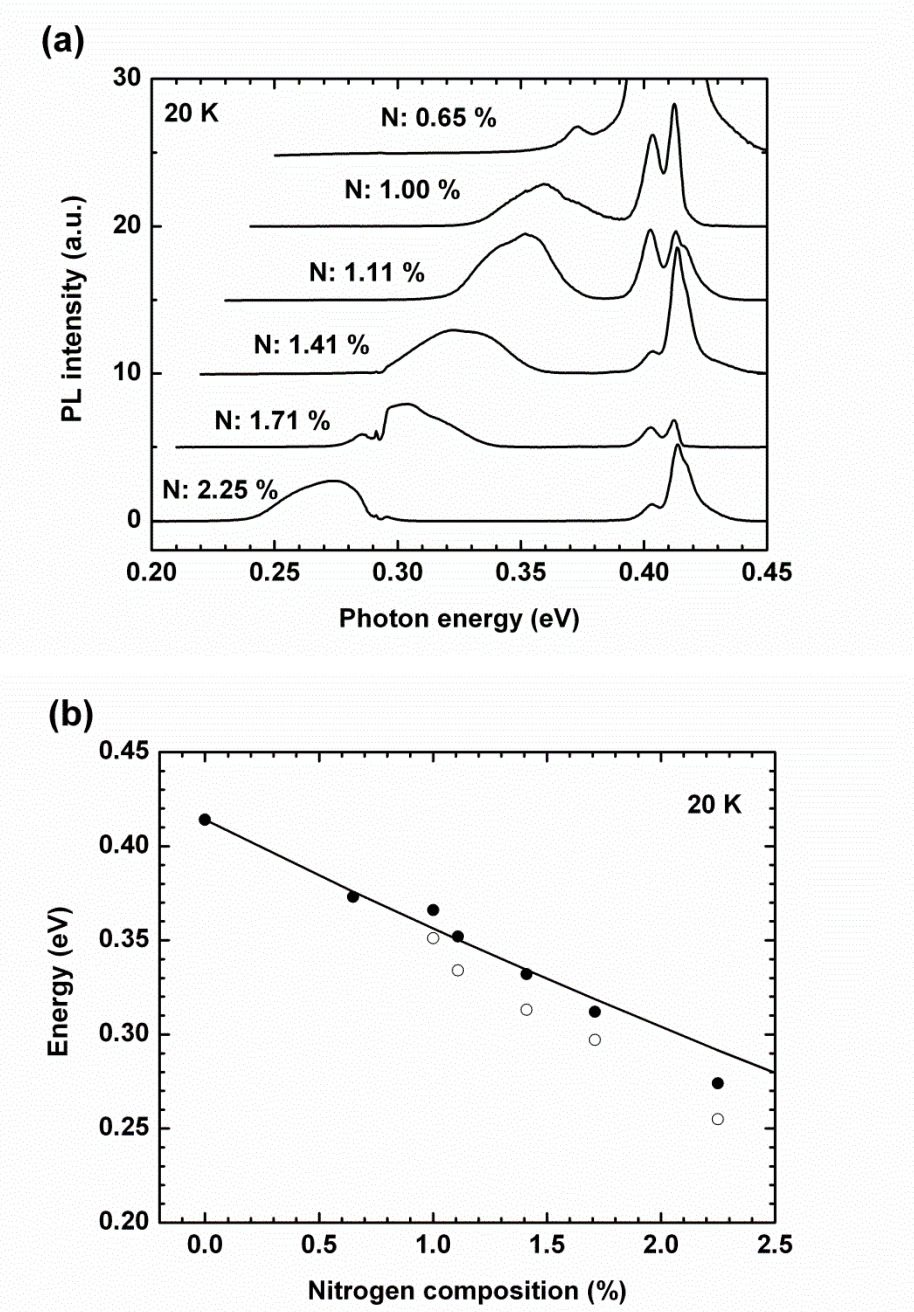

Figure 2.7: (a) PL spectra measured at 20 K for InAsN with variable nitrogen composition. PL band near and above 0.4 eV originates from InAs substrate. The dip near 0.29 eV is CO2 vapor absorption and (b) Dependence of the short and long wavelength PL peak energy on nitrogen composition as measured at 20 K. Solid line is BAC model calculation using parameters from [12].

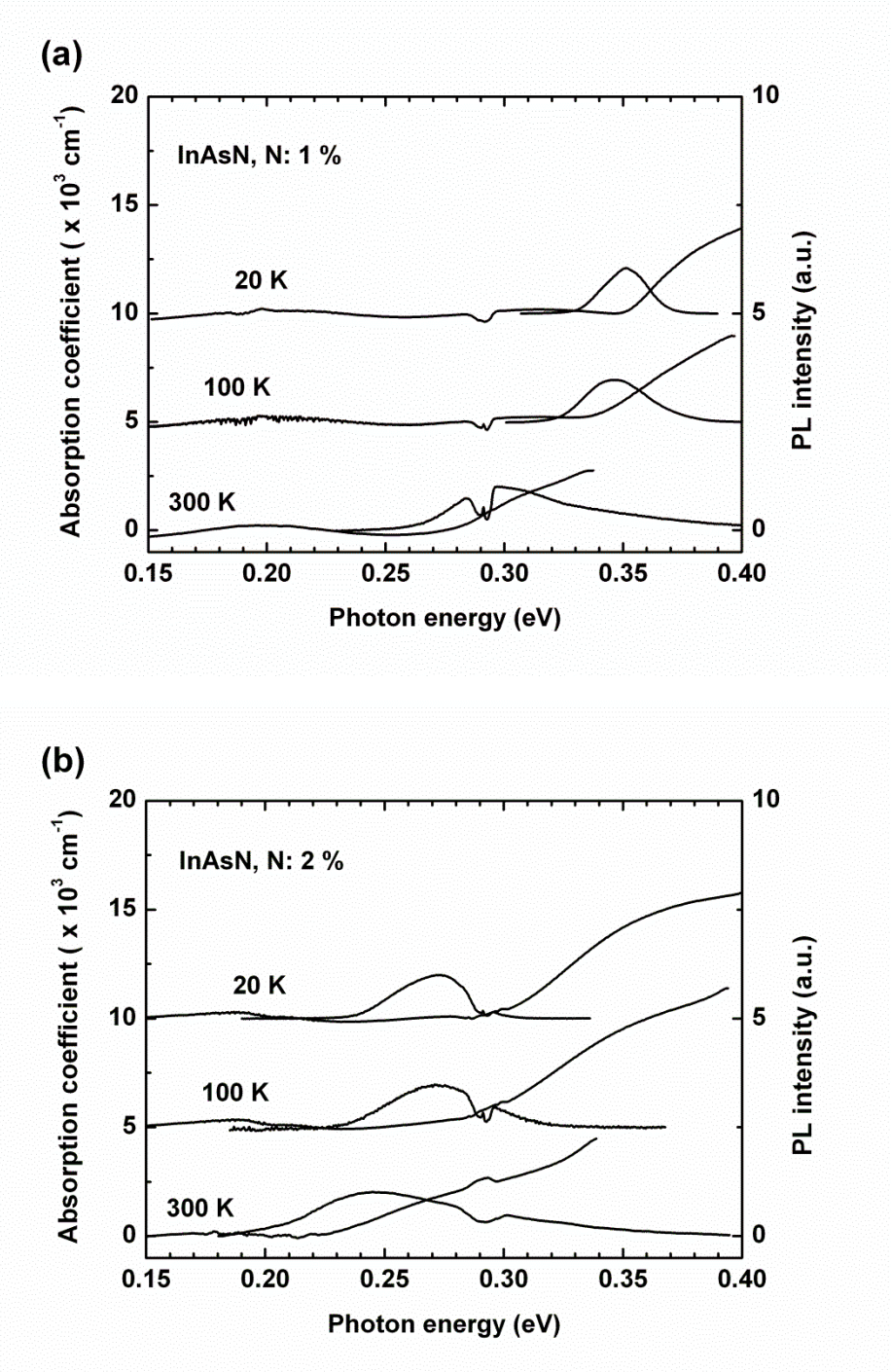

Figure 2.8: PL (thin solid line) and absorption (thick solid line) spectra measured for 1.5 mm-thick InNAs epilayers with 1% (a) and 2% (b) at temperatures equal to 20, 100 and 300 K. The distortion near 0.29 eV caused by CO2 absorption.

more or less successfully fitted using the two-level BAC model [56] at least up to 1.7 % of nitrogen. At elevated temperatures the two-peak nature of the PL spectra becomes smeared and only a single peak can be identified. The overall shift of the PL energy with nitrogen composition is about 55 meV per nitrogen percent at 20 K. Photoluminescence analysis of the thin samples yields roughly the same results as were obtained in [52]. Thus we can conclude that the dilute-nitride InAsN material grown in this work has similar structural properties.

Photoluminescence was complemented by absorption analysis for thick InAsN samples with 1 and 2 % of nitrogen. Optical absorption spectra were determined from transmission measurements using the same approach as in previous section. Figure 2.8 (a) shows the temperature dependence of the absorption edge together with corresponding PL spectra for sample with 1 % of nitrogen. The noticeable fringing of absorption spectra originates from the parasitic Fabri-Perot cavity because of the refractive index steps between InAsN and air/substrate. The absorption edge of InAsN is red shifted from that of InAs by about 50 meV. The close correspondence of the spectral location of the absorption edge and PL peak indicates marginal if any Moss-Burstein shift of absorption spectrum. Indeed, residual carrier concentration of the InAsN with 1 % of nitrogen is expected to be only about 10^{17} cm^{-3} [53], (although it was not directly measured in these samples). For this concentration of electrons (effective mass of about 0.05 of free electron mass [46]) the Fermi level is nearly at the conduction band edge.

For InAsN with nitrogen content of about 2 % (Figure 2.8 (b)) the PL peak is located at energies lower than that of the absorption edge. This difference is most apparent at low temperatures. About 30 meV shift can be ascribed to band filling. The residual carrier concentration in the InAsN sample with 2 % of nitrogen can be roughly estimated from this plausible Moss-Burstein shift as $(5\text{-}10)*10^{17}$ cm^{-3}. At room temperature the 30 meV is comparable to the thermal energy, thus both PL peak and absorption edge occur at about 0.25 eV, i.e. more than 100 meV below the InAs band edge.

Ultra-fast photoluminescence up-conversion was used to study the carrier relaxation dynamics in InAsN bulk materials. The temporal resolution of the experimental technique is about 0.5 ps as estimated from spectrally resolved autocorrelation measurements. Due to the low conversion efficiency of the sum frequency generation the observation of the mid-infrared PL by up-conversion technique usually requires substantial excitation levels. The excitation beam was

focused down to about 10 μm diameter on a sample. The maximum excitation average power was 10 mW, i.e. about 100 pJ/pulse for 80 MHz, 200 fs, 1060nm pulse train. The maximum excitation level corresponds to photo excited carrier concentration around 10^{18} cm^{-3}. This is the free carrier concentration that occurs right after the excitation pulse as calculated from excitation laser beam energy and dimensions. The aforementioned method of calculation of photo excited carrier density obviously lacks accuracy and can serve as one order of magnitude estimation at best.

Figure 2.9 (a) plots a series of PL relaxation curves obtained for the InAsN alloy with 1 % of nitrogen under variable excitation power levels. The PL was recorded at energies near the maximum of the equilibrium PL signal (Figure 2.8 (a)). Based on the approach proposed in [57] we analyzed PL relaxation dynamics using the following equation for total recombination rate R:

$$\mathrm{R}(n)=\frac{1}{n}\frac{\mathrm{d}n}{\mathrm{d}t}\approx\frac{1}{n_0}\frac{\Delta n_0}{\Delta I_{\mathrm{PL}}(n_0)}\frac{\Delta I_{\mathrm{PL}}(n_0)}{\Delta t}=\frac{1}{I_{\mathrm{EX}}(n_0)}\frac{\Delta I_{\mathrm{EX}}(n_0)}{\Delta I_{\mathrm{PL}}(n_0)}\frac{\Delta I_{\mathrm{PL}}(n_0)}{\Delta t} \tag{2.1}$$

where n is excess carrier concentration, t – time, n0 is initial excess carrier concentration right after the excitation pulse, $I_{\mathrm{PL}}(n_0)$ is an intensity of the PL signal corresponding to n_0 (i.e. PL intensity right after excitation pulse), $I_{\mathrm{EX}}(n_0)$ is the excitation pulse energy producing n_0. In equation (1) the local derivatives are replaced by finite difference ratios (denoted by Δ) and linearity between excitation pulse energy and resulting initial excess carrier concentration is assumed. By varying the excitation energy over nearly two orders of magnitude the dependence of the recombination rate on excess carrier concentration was measured at 78 K and at room temperature (Figure 2.9 (b)). In the limit of the vanishing excitation densities the recombination rate R(0) can be used to determine the minority carrier lifetime (τ) according to $\tau = \mathrm{R}(0)^{-1}$. The values obtained are about 2.5 ns at room temperature and about 8.3 ns at 78 K. These values can serve as bottom estimation of the SRH recombination lifetimes since presence of the residual carrier concentration can make radiative and Auger processes contribute. Under several simplifying assumption and for CCHC Auger process the carrier lifetime can be expressed as:

$$\frac{1}{\tau(\Delta n_0)}=A+B(n_{\mathrm{BGR}}+\Delta n_0)+C(n_{\mathrm{BGR}}+\Delta n_0)^2 \tag{2.2}$$

where n_{BGR} is the residual electron concentration and A, B, C are SRH, radiative, Auger recombination constants, respectively. In the limit of the zero excess carrier concentration (Δn_0 =

0) the minority carrier lifetime is determined by the residual doping level and affected by all three recombination parameters (not only by SRH rate as often being implied). The contribution of the Auger process can, for instance, qualitatively explain the increase of the low excitation recombination rate with temperature.

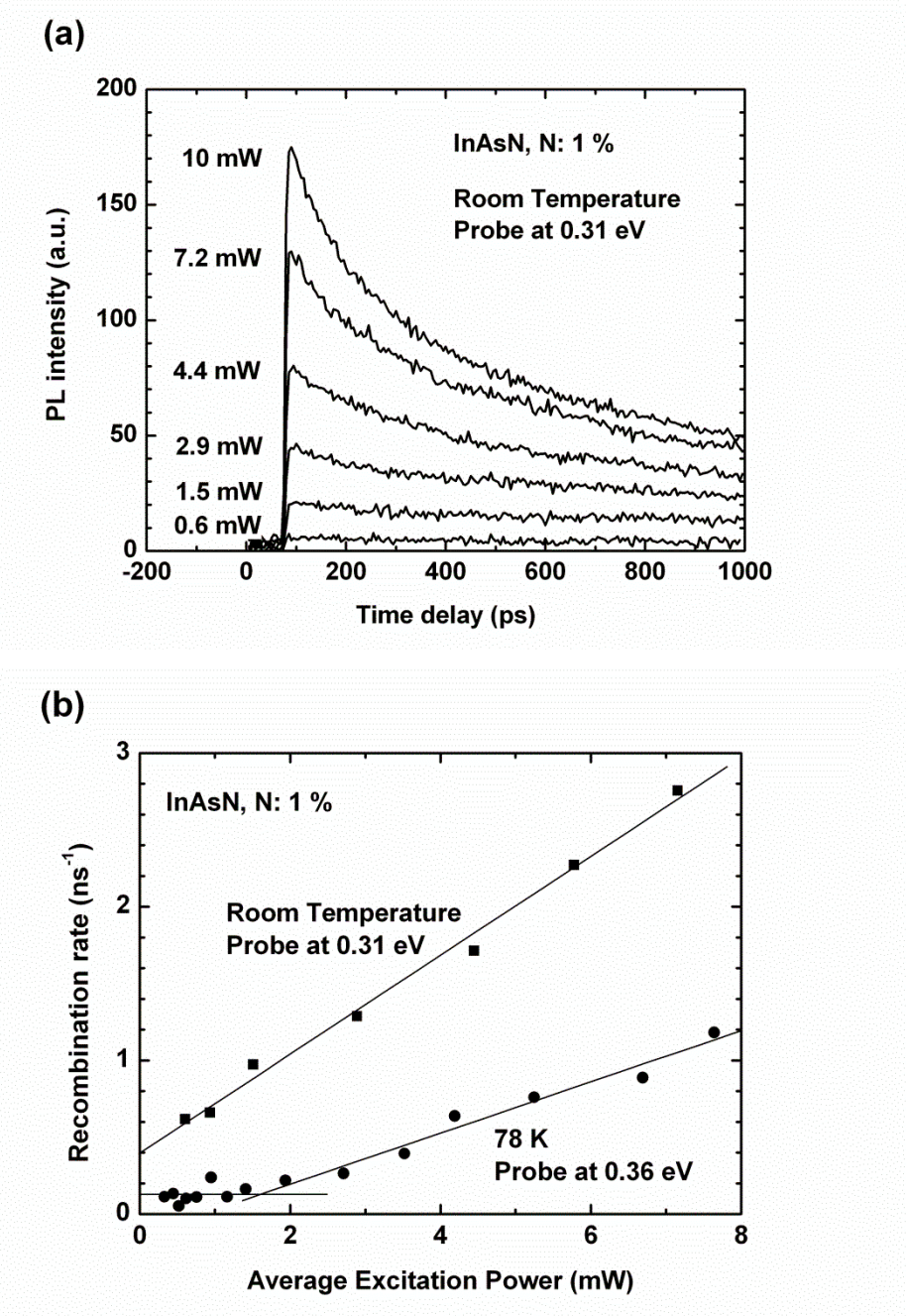

Figure 2.9: (a) PL relaxation curves obtained for InAsN alloy with 1% of nitrogen under several excitation levels and (b) Excitation dependence of the recombination rate for the InAsN alloy with 1% of nitrogen measured at room temperature and at 78 K. Lines are guide for eyes.

Carrier recombination rates increase with excitation level almost linearly. Again, presence of the substantial residual carrier concentration does not allow ascribing this increase to the effect of radiative processes alone. The instant carrier recombination times at high excitation levels are in the range of hundreds of picoseconds, still orders of magnitude better than that observed for GaSbN dilute-nitride materials. The InAsN alloy with 2 % of nitrogen emits PL at room temperature at the wavelength near 4.5 μm which is above the cut off wavelength of our experimental setup. At 78 K the PL signal was measured and low excitation carrier lifetime of about 5 ns was determined.

Summarizing, InAsN bulk materials were grown by MBE with nitrogen contents of up to 2.25 %. Photoluminescence measurement show that the bandgap energy decreases continuously from that of InAs by nearly 150 meV when nitrogen content is increased up to 2.25 %. Comprehensive absorption and photoluminescence spectroscopy analysis demonstrates Moss-Burstein shift below 30 meV for nitrogen content of 2 %. The separation of the PL and absorption edge is apparent only at low temperatures and for sample with 2 % of nitrogen. The low excitation minority carrier lifetimes at 78 K decrease from about 8 to about 5 ns when nitrogen content is increased from 1 to 2 %. At elevated temperatures the minority carrier lifetime decreases from 8 to 2.5 ns for nitrogen content of 1 %. More than three orders of magnitude improvement in minority carrier lifetime is observed in unoptimized InAsN material as compared to GaSbN, encouraging further optimization of the former for detector applications. Difference in energetic position of the nitrogen complex states can be responsible for the observed difference.

Chapter 3 Development of unstrained and unrelaxed InAsSb alloys

GaSb based III-V materials are widely used in the development of mid- and long-wave infrared optoelectronic devices because of the narrow bandgap and the flexibility in forming heterojunctions with various types of band offsets, i.e. type I, type II staggered or type II broken gap. For device applications, heterostructures with a considerable thickness are preferably grown lattice-matched or nearly lattice-matched to the substrate. Therefore, the device design is restricted by the lattice parameters of commercially available III-V substrates. For example, in the case of GaSb based type I lasers, the content of As in InGaAsSb quantum wells must be high enough to satisfy the conditions of pseudomorphic growth, but high As content in quantum wells severely affects the device performance [58]. In principle, the problem can be addressed by the epitaxial growth of lattice-mismatched materials of the desired lattice parameters.

The key issue in mismatched epitaxy is to minimize the dislocations that penetrate through the epi-structures. In this work, we expand the lattice parameter of the GaSb substrate by growing linearly compositionally graded Ga(Al)InSb buffers, following the approach in [59, 60]. The graded strain in the buffer layers facilitates the glide of threading dislocations and reduces the densities of dislocations that propagate through the buffer layer into the device [59]. High quality $InAs_{1-x}Sb_x$ layers having non-tetragonally distorted, strain-free lattice parameters were grown on top of the buffer layers with thickness up to 1.5 μm.

$InAs_{1-x}Sb_x$ alloys are of special interest, because the bowing effect in the band gap *Eg* is dependent on the Sb composition, which allows the growth of layers having bandgaps narrower than that in InSb [61, 62, 63, 64, 65, 66]. In the second section of this chapter, we present the optical properties of non-distorted $InAs_{1-X}Sb_X$ alloys grown on linearly compositionally graded Ga(Al)InSb buffers. Strong PL was observed for $InAs_{1-X}Sb_X$ alloys in a wide temperature range. A relatively long carrier lifetime was obtained in $InAs_{0.8}Sb_{0.2}$ alloys from the PL response to modulated optical excitation.

3.1 Structural characterization of metamorphic InAsSb alloys and buffers

The heterostructures were grown on GaSb substrates by solid-source molecular beam epitaxy using a Veeco GEN-930 system equipped with As and Sb valved cracker sources.

Molecular beam fluxes were measured by an ion gauge positioned in the beam path. The substrate temperature was controlled by a pyrometer, which was calibrated using references such as the III to V enriched surface reconstruction transition, oxide desorption and the melting point of InSb. The compositionally graded 2~3.5 μm thick Ga(Al)InSb buffer layers were grown at temperatures ranging from 460 to 520 ˚C. The growth temperature was maintained near 415 ˚C for the InAsSb layers. The Sb incorporation was controlled by the adjustment of the relative pressure of the As and Sb group V elements as measured by the beam-flux-monitor. The growth rate was about 1 μm per hour. $InAs_{1-X}Sb_X$ layers with x = 20, 30 and 44% were grown on GaInSb and AlGaInSb buffers.

The defect distribution in linearly compositionally graded GaInSb and AlGaInSb buffers were characterized by cross-sectional TEM images. Figure 3.1 shows the XTEM images of structures with either laser or absorber layers grown on top of three different linearly graded buffer layers; including (a) GaInSb with top In content of 16%; (b) GaInSb with top In content of 30%; (c) AlGaInSb with top Al, Ga and In contents of 75, 0 and 25 %, respectively. The images were taken with a (220) bright field two-beam condition to emphasize the dislocations. In all three structures, the misfit dislocation network was confined in the bottom part (~1.5 μm) of the graded buffers; the topmost portion of the buffers as well as the epi-structures grown onto the buffers is free from misfit dislocations. TEM results did not show any noticeable difference in the dislocation morphology of these two buffer layers or in the laser or absorber layer structures

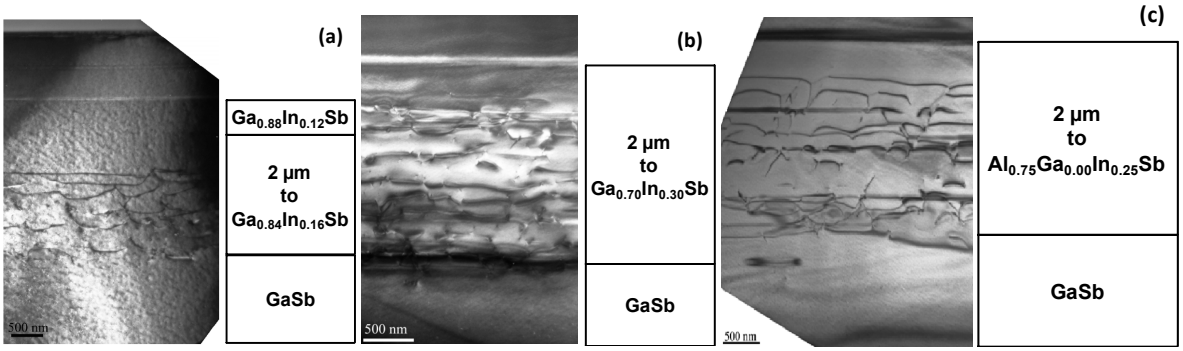

Figure 3.1: Cross-sectional TEM images of samples with 2 µm thick linearly graded buffers grown on GaSb substrates: (a) GaInSb with top In content of 16 % - mismatch accomodated 0.9 %; (b) GaInSb with top In content of 30 % - mismatch accomodated 1.4 %; (c) AlGaInSb with top Al, Ga and In contents of 75, 0 and 25 % - mismatch accomodated 1.4 %.

grown on top of them, both appear to be equally efficient in accommodating the misfit strain. From the images, we can estimate that the threading dislocation density is below 10^7 cm^{-2} in the $InAs_{1-X}Sb_X$ layers.

The surface morphology was characterized by atomic force microscopy (AFM) in tapping mode (AFM Dimension V). Cross-hatched patterns with crossing lines along the [110] crystallographic directions were observed on all structures. However, structures grown on AlGaInSb buffers showed better surface morphology. Figure 3.2 (a) and (b) show the AFM amplitude images measured over a 50 by 50 μm area for samples with $InAs_{0.8}Sb_{0.2}$ layer grown on a (a) GaInSb buffer and a (b) AlGaInSb buffer. The undulation amplitude and period in sample (a) were about 10 nm and 9 μm, respectively, both nearly twice as much the ~ 5nm and ~ 5 μm measured for sample (b). Figure 3.2 (c) shows the image of sample (b) measured over 3 by 3 μm area; the root mean square surface roughness, i.e., in between of the dips in cross-hatch pattern, was below 1 nm. Increasing the Sb content led to larger peak-to-peak variations in the cross-hatch pattern, as indicated by surface roughness up to 10 nm for the $InAs_{0.56}Sb_{0.44}$ samples.

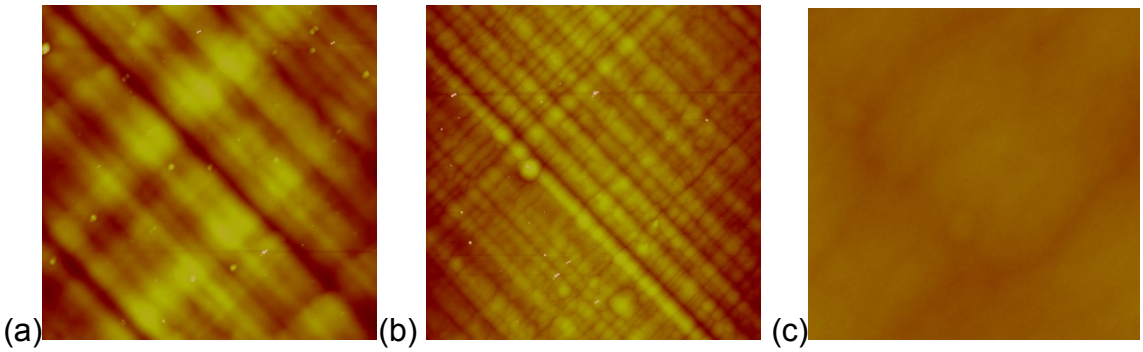

Figure 3.2: AFM amplitude images measured over 50 by 50 μm area for samples with $InAs_{0.8}Sb_{0.2}$ layer grown on (a) GaInSb buffer and (b) AlGaInSb buffer; (c) shows the enlarged image (3 by 3 μm) of sample (b).

Strain relaxation of the structures was examined using high-resolution X-ray diffraction reciprocal-space mapping (RSM) at the symmetric (004) and asymmetric (335) Bragg reflections. Figure 3.3 presents a set of RSM measurements for a structure consisting of a 1 μm $InAs_{0.8}Sb_{0.2}$ layer grown on a 2 μm linearly compositionally graded AlGaInSb buffer layer. The

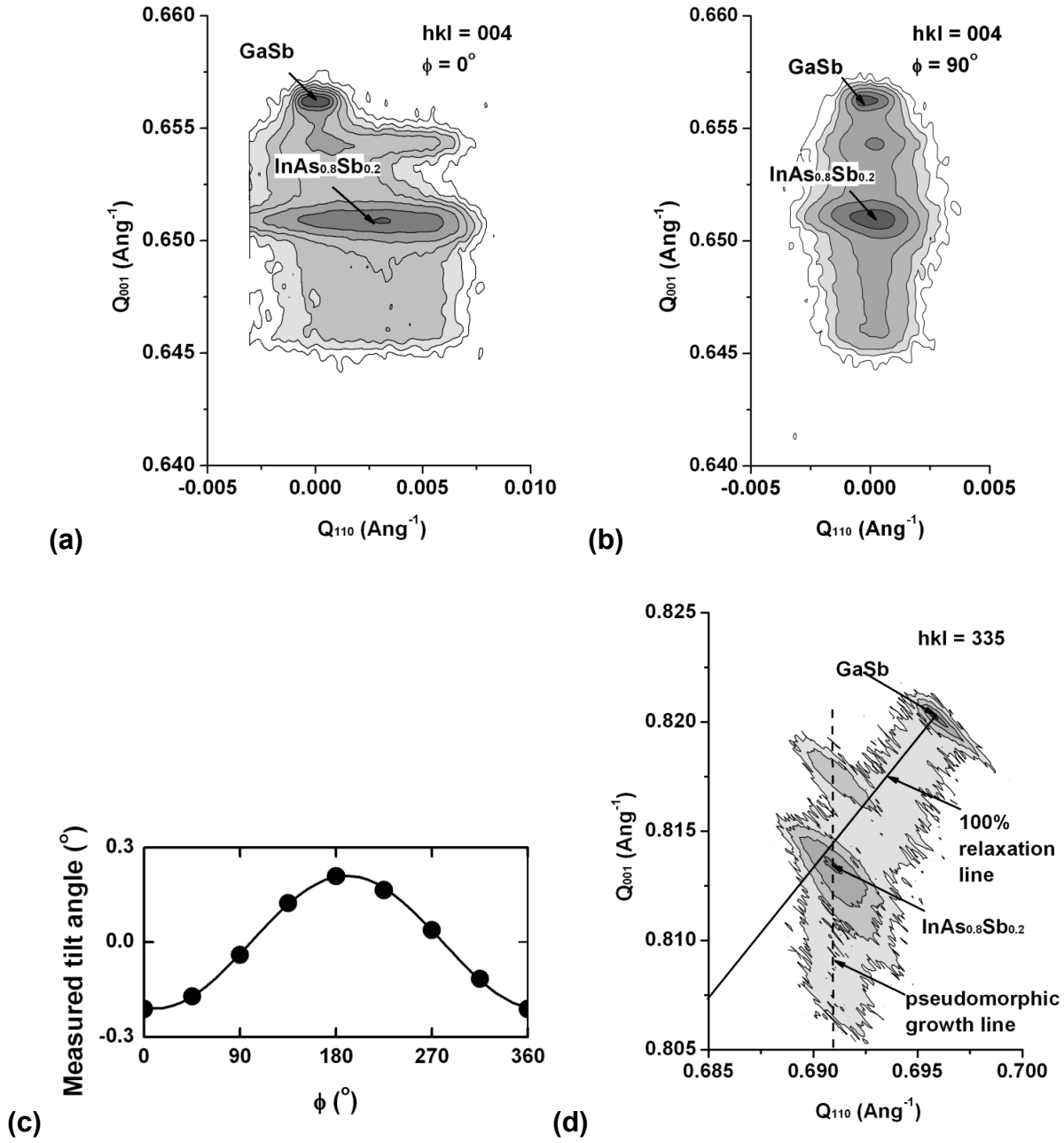

Figure 3.3: (a) Symmetric (004) RSM taken at the azimuth angle emphasizing the tilt in the epi-layers; (b) (004) RSM taken at the azimuth angle minimizing the tilt in the epi-layers; (c) dependence of the measured tilt angle as a function of the azimuth angle; (d) asymmetric (335) RSM taken at azimuth angle equal to 90˚. Solid line denotes the location of 335 reflexes corresponding to fully relaxed material with lattice parameter gradually increasing from that of GaSb. Dashed line denotes the location of 335 reflexes of the material with further increasing native lattice parameter but grown pseudomorphically to the top of fully relaxed section.

native lattice constant of the $InAs_{0.8}Sb_{0.2}$ layers is about 0.8% larger than that of GaSb. The native lattice constant of the buffer layer changed from that of GaSb to that of $Al_{0.75}Ga_{0.13}In_{0.12}Sb$ with a strain ramp rate about 0.6% per μm. The topmost section of the graded buffer with $Al_{0.75}Ga_{0.13}In_{0.12}Sb$ composition had a native lattice constant about 1.3% larger than that of GaSb, but due to compressive strain, the in-plane lattice constant is equal to the native constant of the bulk $InAs_{0.8}Sb_{0.2}$. When the final structure was grown, the InAsSb layer was sandwiched between $Al_{0.75}Ga_{0.13}In_{0.12}Sb$ carrier confinement layers to assist photoluminescence experiments.

The symmetric reflection revealed the tilt present in the epi-structure. Figure 3.3 (a) and (b) shows the RSMs obtained near the symmetric (004) reflection at two azimuth angles, namely (a) $\varphi = 0^\circ$ and (b) $\varphi = 90^\circ$, corresponding to two perpendicular [110] crystallographic directions. The tilt angle projected to the measurement plane is determined from the horizontal peak separation between the GaSb substrate and the epi-layers. As shown in figure 3.3 (a), the tilt angle increases as the thickness increases in the bottom part of the graded buffer, and stops increasing in the consequent layers. The bottom part of the buffer layers is near completely relaxed, as will be shown later, suggesting that tilting is associated with the process of strain relaxation. Figure 3.3 (c) plots the projected tilt angle as a function of several azimuth angle φ. We estimate the tilt angle to be 0.2° in the direction about 10° away from the [110] direction ($\varphi = 90^\circ$).

Asymmetric (335) RSM reflexes were measured at four different azimuth angles in order to characterize the degree of relaxation of the graded buffer layer and to confirm that the $InAs_{0.8}Sb_{0.2}$layer is lattice-matched to the topmost part of the graded buffer. Figure 3.3 (d) shows one of the (335) RSMs measured at an azimuth angle equal to 90°, i.e., with the minimum tilting effect. The shift visible in the (335) RSM corresponds to the transition from the strain relaxed to the pseudomorphic section of the graded buffer. For illustrative purposes, the solid line corresponds to a 100% relaxed square lattice. The observed relaxation is close to 100%. After the tilt angle is accounted for, the degree of relaxed in this section of the graded buffer can be estimated as 95%, i.e., nearly 100%, and within our experimental error. The pseudomorphic growth of the dislocation-free topmost section of the buffer layer is apparent from the (335) scan since the reflex from the buffer layer is nearly vertical (dashed line in figure 3.3 (d)). The reflection from the $InAs_{0.8}Sb_{0.2}$ layer is located at the turning point and on the same vertical line as the pseudomorphic section of the buffer, which confirms lattice matching to the in-plane lattice constant of the graded buffer layer. The amount of strain in the $InAs_{0.8}Sb_{0.2}$ layer is below

0.1%; therefore, no strain relaxation is expected. The reflection located above the InAsSb reflection in both the (004) and (335) RSM corresponds to a pseudomorphically strained auxiliary AlGaSb layer (~150 nm) that was grown on top of the InAsSb layer for calibration purposes.

3.2 Optical characterization of InAsSb alloys

The PL and absorption spectra were measured with a Fourier-transform infrared (FTIR) spectrometer equipped with a liquid-nitrogen cooled HgCdTe detector with a cut-off wavelength of 12 μm. The PL was excited by either a 970 nm laser diode or a Nd:YAG laser and collected by reflective optics. PL was observed from all structures in a wide temperature range, up to room temperature from samples with 20% Sb. Figure 3.4 (a) shows the PL spectra from 1-μm thick $InAs_{0.8}Sb_{0.2}$ layer grown on an AlGaInSb buffer at 13, 150 and 300 K. Figure 3.4 (b) presents the PL spectra measured from a 1-μm thick $InAs_{0.56}Sb_{0.44}$ layer grown on an AlGaInSb buffer and a 1.8-μm thick long-wave InAs/GaSb superlattice grown on a GaSb substrate. The superlattice structure consists of 300 periods of InAs and GaSb layers with the cell period of 63 Å enclosed within 20-nm AlAsSb carrier confinement layers lattice-matched to GaSb. The spectral widths (full-width at half maximum) for the three samples were similar, about 11 meV. The PL intensities from both $InAs_{0.56}Sb_{0.44}$ and superlattices were comparable at 13 K while intensities drops much faster in InAsSb sample at elevated temperatures. Considering the challenge of creating adequate hole confinement in the As-rich alloys, the faster drop of the PL intensity with temperature can be explained by the increased diffusion of the excess carriers out of the InAsSb layer.

The absorption spectra were measured for the InAsSb layers with Sb compositions of 20% and 30% grown on GaInSb buffers. The absorbance was determined from transmission measurements taking into account the multiple reflections. The absorption spectrum was derived by subtracting the absorbance of the heterostructure with the epi-layers and the substrate. The transmission of the substrate was determined using the same sample after the epi-layers were removed by polishing. The substrate of the sample with 20 % Sb was thinned to 300 μm. The substrate of the heterostructure with 30 % Sb was lapped down to near 50 μm thickness because of high free carrier absorption in the GaSb at longer wavelengths. The latter was determined to be 140 cm^{-1} near λ = 8 μm for the GaSb substrates with Te doping level of 3×10^{18} cm^{-3}. The

sample with the measured thickness of 55 μm had near 50 % transmission at this wavelength, as compared to a 2 % transmission for the 300 μm-thick substrate. The free carrier absorption in the thin substrate was determined by a fit based on the absorption measurements for the thicker substrate. Both absorption and PL spectra measured for the two samples at 150 K are presented

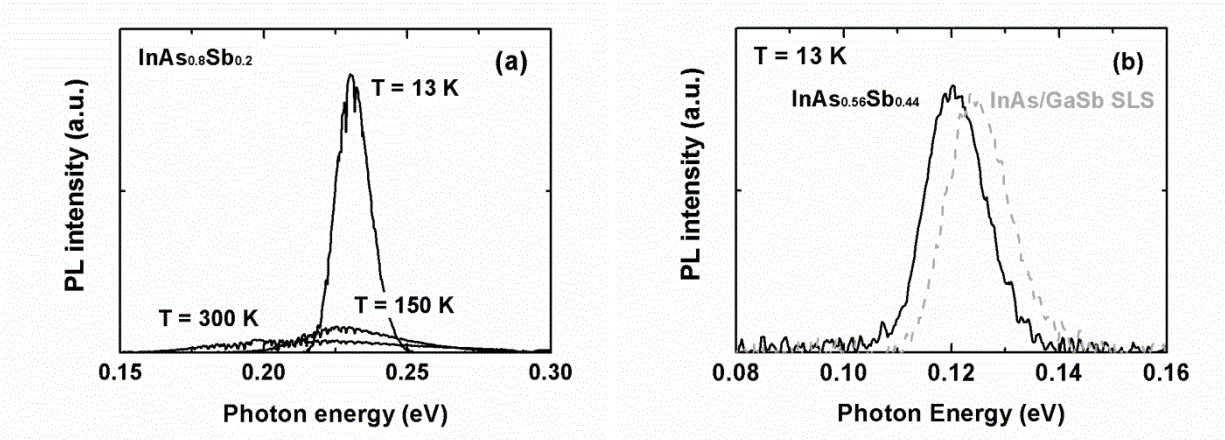

Figure 3.4: (a) PL spectra from $InAs_{0.8}Sb_{0.2}$ sample grown on AlGaInSb buffer at 13 K, 150 K and 300 K under an excitation power of 0.5W. (b) PL spectra from $InAs_{0.56}Sb_{0.44}$ layer grown on AlGaInSb buffer and long-wave InAs/GaSb superlattices grown on GaSb substrate at 13 K under an excitation of 0.1 W. The PL was excitation by a Nd:YAG laser with a beam diameter of about 0.5 mm.

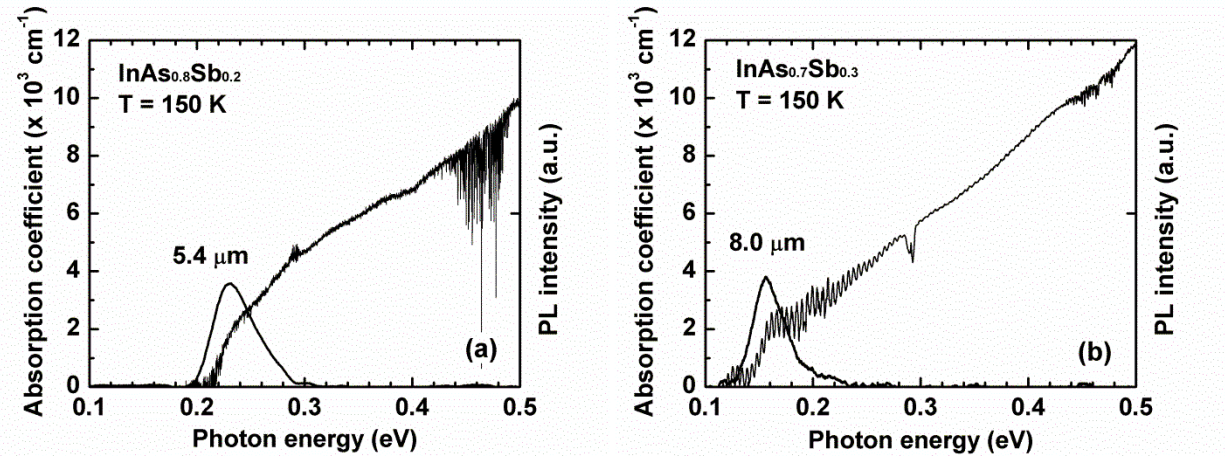

Figure 3.5: Absorption and PL spectra measured at 150 K for (a) $InAs_{0.8}Sb_{0.2}$ and (b) $InAs_{0.7}Sb_{0.3}$. The PL was excited by a 970-nm laser diode at a power of 400 mW; the excitation area was 2.5 x 10^{-3} cm^2. The distortion near 0.29 eV was caused by CO2 absorption.

in Figure 3.5. The PL peak energy matched the absorption edge indicating that the PL was associated with the band-to-band recombination.

The energy positions of PL maxima at T = 13 K versus Sb composition x in the InAsSb layers are presented in Figure 3.6. The positions of PL maxima were used to determine the bandgaps and the bowing parameter, which was about 0.9 eV, considerably greater than the recommended value of 0.7 eV [1]. The lower value of bowing reported previously was based on measurements in materials grown without control of the strain relaxation. The observed difference in the bowing between the 0.9 eV determined in this work and the 0.7 eV reported in literature can be explained by the absence of residual strain in the InAsSb epitaxial layers.

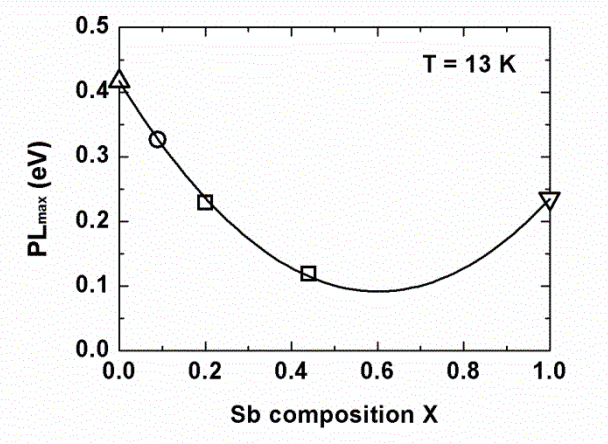

Figure 3.6: Dependence of 13K PL maxima on composition X in InAs1-XSbX epitaxial layers: InAs epilayer grown on InAs substrate (triangle), InAsSb0.08 epilayer grown lattice matched to GaSb substrate (circle), InAs1-XSbX epilayers grown on AlGaInSb buffers (squares) on GaSb substrate, InSb epilayers grown on InSb substrate (inverted triangles).

Carrier lifetime measurements for the 1-μm thick $InAs_{0.8}Sb_{0.2}$ layer grown on AlGaInSb buffer layer were performed at T = 77K using optical modulation response technique [67]. To minimize the effects of carrier separation on the carrier lifetime in undoped InAsSb layers, the Al0.25Ga0.70In0.05Sb barriers were doped with Be to the level of 1×10^{17} cm^{-3}. The dependence of the carrier lifetime on the excitation power is shown in figure 3.7. The carrier lifetime was determined from the PL response to a small signal modulation of excitation in the frequency domain. The PL response spectra in a range of cw exc itation power are shown in figure 3.7(a). The carrier lifetime τ corresponding to the cut-off frequency (-3dB point) was

obtained by fitting the response in the entire frequency range to the dependence $PL_\omega \propto [1 + (2\pi f \times \tau^2)^2]^{-1/2}$. A 250 ns carrier lifetime under low excitation condition was measured. The excess carrier concentration was estimated to be in the range $(2\sim4)\times10^{15}$ cm^{-3} at the excitation power in

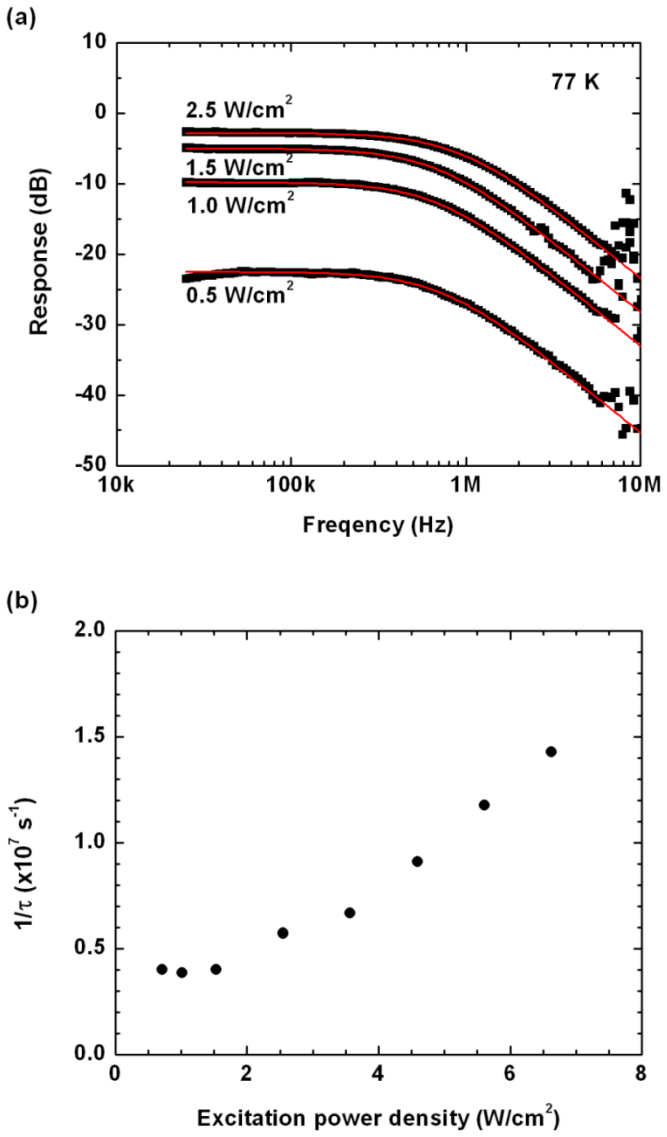

Figure 3.7: Carrier lifetime measurements at T= 77 K on a 1-μm-thick $InAs_{0.8}Sb_{0.2}$ layer grown on an AlGaInSb buffer on a GaSb substrate. (a) The PL responses and fits are presented for continuous wave excitation power levels of 0.8, 1, 1.4, 3 and 5 mW from bottom to top, respectively. The PL was excited at the wavelength of 1.31 μm, and the excitation area was 2×10^{-3} cm^2 FWHM. (b) The reciprocal carrier lifetime is plotted versus continuous–wave excitation power density.

the range of 0.5~1 W/cm^2.

In summary, we conclude that growing compositionally graded buffers (Ga(Al)InSb on GaSb substrates) with a strained but unrelaxed top layer allows the fabrication of bulk $InAs_{1-x}Sb_x$ layers (0.5~1.5 μm thick). These films have characteristics that are promising for the development of IR detectors operating within the spectral range from 5 to 12 μm. The critical element of the technology is the control of the in-plane lattice constant of the topmost section of the buffer. The in-plane lattice constant of this layer must be equal to the lattice constant of $InAs_{1-x}Sb_x$ with given x. The unrelaxed $InAs_{1-x}Sb_x$ epitaxial layers grown on top of such buffers demonstrated photoluminescence in the spectral range from 5.2 to 9.4 μm within the temperature range of 77~150 K. The carrier lifetime of 250 ns was obtained at T = 77K for structure consisting $InAs_{0.8}Sb_{0.2}$ epi-layers.

Chapter 4 Development of light emitting diodes and photodetectors using InAsSb alloys

4.1 Light emitting diodes using bulk InAsSb active regions

The development of highly efficient light emitting devices and detectors operating in the spectral region above 5 μm using III-V fabrication technology remains an important task. Infrared (IR) light emitting diodes (LEDs) have potential applications such as pollutant gas sensing, molecular spectroscopy, process monitoring, noninvasive disease analysis, and infrared scene projection [68, 69, 20]. IR photodetectors have broad applications in imaging, and environmental and industrial monitoring [70]. Type-II superlattices (T2SLs) are a key structure used in IR devices designed for these technologies. However, not all IR device design requirements can be satisfied by using T2SLs. The short minority carrier lifetimes of $\tau < 100$ ns [71] in InAs/Ga(In)Sb T2SLs are detrimental to the performance of photodetectors due to their effects on the dark current. InAs/$InAs_{1-x}Sb_x$ structures with interband optical transitions near 10 μm are characterized by longer minority lifetimes $\tau \sim 400$ ns [72], but the growth of these structures requires the utilization of thick layers of InAs [72, 73]. The latter suppresses the interband optical coefficient [73, 74] and impedes hole transport along the growth direction. The hole transport limitation and the low value of the interband matrix element of the active layer affect the performance of LEDs and nBn type "barrier" detectors.

All these challenges can be overcome by using InAsSb bulk layers in the active regions of the device heterostructures. The bandgap of the InAsSb alloys can be tailored in a range from below 100 meV to above 300 meV by choosing the group V element content [75, 76]. However the growth of an alloy with a fundamental absorption edge in the vicinity of 10 μm requires about 40% Sb composition and implies a lattice mismatch of about 2~2.5% with respect to the GaSb or InSb substrate.

In the previous chapter we have demonstrated that by using a compositionally graded buffer, high quality InAsSb bulk layers can be grown on a virtual substrate with lattice constants up to 2.1% larger than that of GaSb. The structural, recombination, and optical characteristics of these layers were described in [77]. This approach opens the opportunity of developing new types of barrier optoelectronic devices for the spectral region near and above 5μm. The active

region of these emitters and detectors will be potentially free from the fundamental transport and optical transition limitations associated with InAs/$InAs_{1-x}Sb_x$ materials.

In this section, we will discuss the characteristics of heterostructures containing bulk $InAs_{1-x}Sb_x$ and lattice matched AlInAsSb barriers. The structures were grown on graded InGaSb buffers on GaSb substrates. Devices with $InAs_{1-x}Sb_x$ layers having x=0.2 and x=0.44 operated in LED mode at 80K demonstrated output powers up to 90 μW and 8 μW at 5 μm and 8 μm, respectively.

The structures were grown by solid-source molecular beam epitaxy in a Veeco Gen-930. The growth details were described in [78]. The composition of the GaInSb buffer was linearly graded over 2 μm to $GaIn_{0.8}Sb_{0.2}$ or over 3 μm to $GaIn_{0.6}Sb_{0.4}$. Then 500 nm thick $Ga_{0.87}In_{0.13}Sb$ or $Ga_{0.64}In_{0.36}Sb$ virtual substrates were grown with their native lattice parameters matched to the in-plane lattice parameter of the top strained part of the buffer. Finally, the InAsSb/AlInAsSb/InAsSb heterostructure was grown on top lattice matched to the virtual substrate.

The lattice parameters of the individual layers in the metamorphic heterostructures were quantified by high resolution X-ray diffraction analysis. Figure 4.1 shows the reciprocal space maps (RSM) measured near the asymmetric (335) reflex of the GaSb substrate. The RSM measurements were performed at 0 and 180 degrees azimuthal angles with respect to the [110] direction. The [110] and [-1-10] RSM data were averaged to compensate for the tilt of the metamorphic layers with respect to the GaSb substrate [77]. The line drawn through the reflex from the GaSb substrate corresponds to the (335) reflexes of an ideal, completely relaxed cubic lattice with an increasing lattice constant. It can be seen that the bottom portion of the compositionally graded buffer has cubic symmetry, i.e. it is nearly 100% relaxed, since the corresponding reflexes are grouped around the line drawn through the GaSb (335) reflex. The top part of the compositionally graded buffer is pseudomorphically strained and has a constant in-plane but an increasing out-of-plane lattice parameter. The active region heterostructure layers grown on top of the compositionally graded buffers produce peaks in RSM which are located near the intercept of the 100% relaxation and the vertical line corresponding to the top portion of the grade.

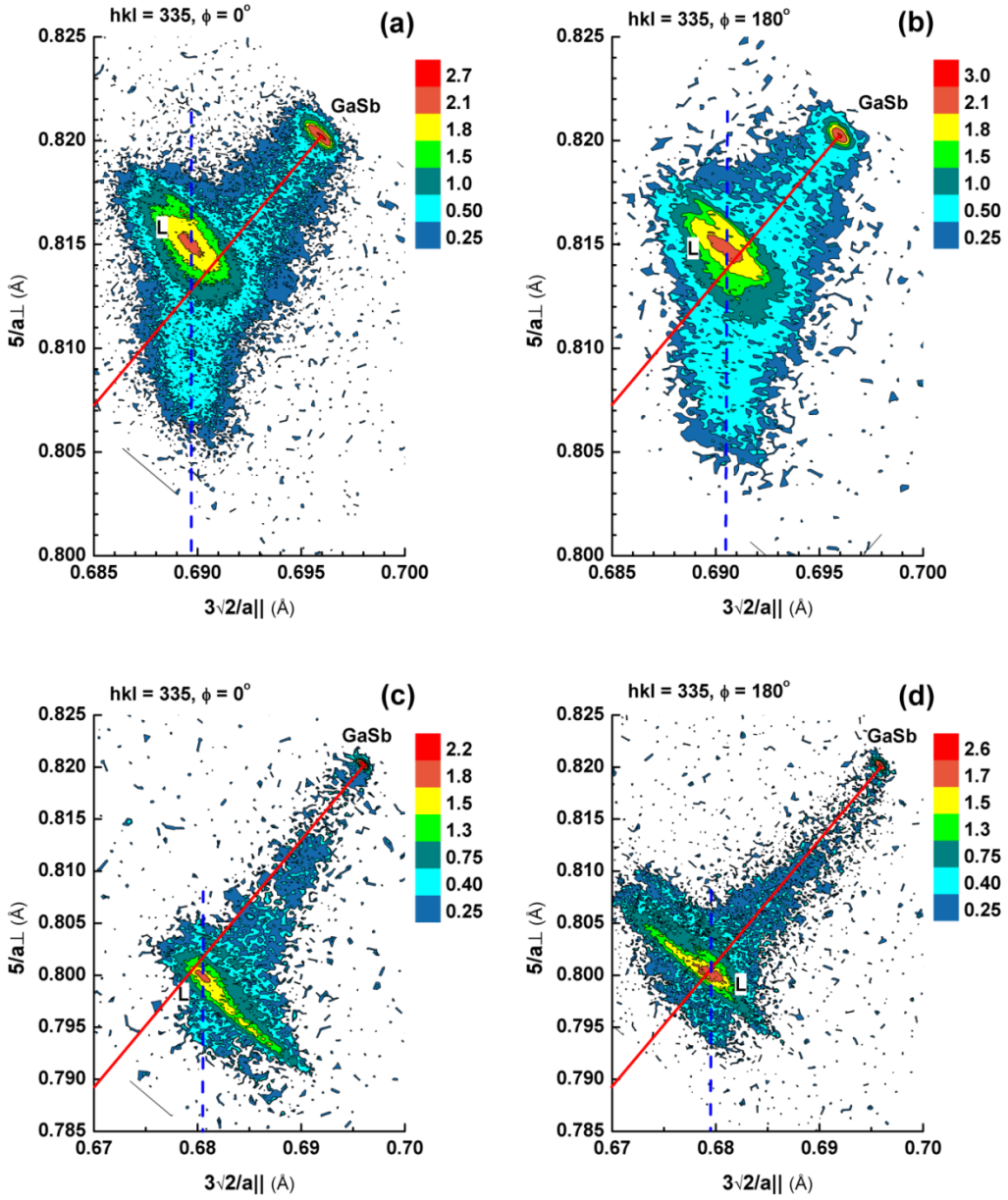

Figure 4.1: Asymmetric (335) RSMs measured for structures with $InAs_{0.8}Sb_{0.2}$ (a, b) and $InAs_{0.56}Sb_{0.44}$ (c, d) in the [110] and [-1-10] directions. The reciprocal lattice point corresponding to the 1-μm-thick InAsSb layer is marked as L. The solid red line denotes the location of 335 reflexes of fully relaxed materials and the vertical dashed blue line denotes that of the materials grown pseudomorphically on top of the buffer. Shown in the legend is the common logarithm of the x-ray intensity in the unit of counts/s.

Thus, we conclude that the heterostructure is nearly undistorted cubic and is grown pseudomorphically to the in-plane lattice parameter of the compositionally graded buffer layer. The amount of residual strain in the heterostructure was determined by direct measurement of the in-plane (100) and (010) and perpendicular (001) lattice parameters from the RSM data. Using a linear interpolation for the c_{11} and c_{12} elastic constants [1] and the standard relationship between strains in perpendicular directions ($\varepsilon_{\square} = -2\frac{c_{12}}{c_{11}}\varepsilon_{\|}$) [79] we determined the residual strains and composition of the $InAs_{1-x}Sb_x$ layers. The residual in-plane strain for the sample with the $InAs_{0.8}Sb_{0.2}$ layer is 0.09%, while the sample with the $InAs_{0.56}Sb_{0.44}$ layer exhibited a residual in-plane strain of 0.08%. Low residual strain values imply no relaxation and thus no formation of new misfit dislocations in the heterostructure layers. This is confirmed by RSM results showing that peaks from InAsSb are located on the same vertical line as the cloud of reflexes from the pseudomorphic part of the compositionally graded buffers.

To obtain information about electroluminescence characteristics, two different metamorphic InAsSb/AlInAsSb heterostructures were designed and grown on InGaSb buffers. The corresponding layer compositions, thicknesses and doping profiles are presented in Table I. Figure 4.2 shows an example of the schematic band diagram for the LED structure with x= 0.2. The composition of the quaternary barrier layer was chosen to align the valence band to that of the InAsSb.

The wafers were processed into LEDs as follows. The epilayer side of all structures was covered with a 300 nm thick silicon nitride dielectric layer. Windows of 400 μm diameter were opened in the dielectric and a top Ti/Pt/Au metal contact was deposited. The wafers were lapped down to about 200 μm; Ni/Au/Ge/Ni/Au was deposited on the n-GaSb substrate and annealed followed by Ti/Pt/Au n-side metallization. Electroluminescence was collected through 500 μm diameter windows in the n-side metallization. No antireflection coating was applied. The LEDs were cleaved into 600 μm x 600 μm squares.

Figure 4.3 shows the electroluminescence spectra and LED output power for structures with x=0.2 (a, b) and 0.44 (c, d) respectively. The structure with x=0.2 exhibited 90 μW total emitted power at a wavelength around 5 μm at 77 K and 10 μW at room temperature. The structure with x=0.44 emitted 8 μW at 77 K at a peak wavelength of about 8 μm. The blue shift of the energy position of electroluminescence peak in Figure 4.3(c) (for x=0.44, $E_g \leq 0.120$ eV [10]) is explained by band filling under electrical injection.

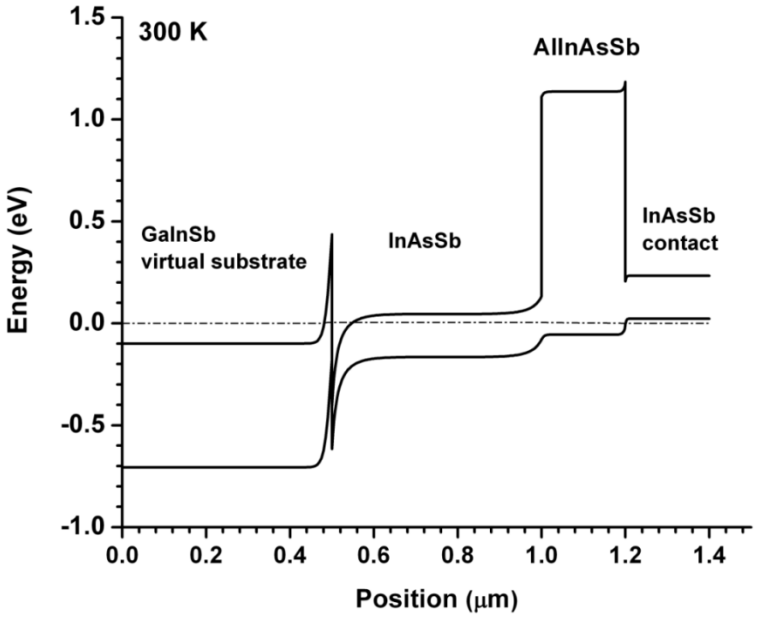

Figure 4.2: Schematic band diagram for an LED with x=0.2 at zero bias. It consists of a 500 nm nominally undoped $InAs_{0.8}Sb_{0.2}$ active layer, a 200 nm Be-doped (p: 1×10^{18} cm^{-3}) $Al_{0.6}In_{0.4}As_{0.29}Sb_{0.71}$ barrier and a 200 nm heavily Be-doped (p: 1×10^{19} cm^{-3}) $InAs_{0.8}Sb_{0.2}$ contact layer. The dash-dot line denotes the Fermi level.

The optical power was measured using calibrated indium-antimonide and mercury-cadmium-telluride photodetectors. All light emitted from the LED surface was coupled to one aperture of a gold-plated integrating sphere with a photodetector mounted in another aperture, thus no assumptions about the LED's direction diagram had to be made. The photodetector-integrating-sphere setup was calibrated using a black-body source operated at 800 ^{0}C. The emission of the black-body was sent through an 8 mm diameter aperture and was measured using a calibrated thermopile photodetector, and used for photodetector calibration. Spectra of the photodetector responsivity and LED electroluminescence were measured by Fourier Transform and grating spectrometers.

The output power of the 8 μm LEDs with 0.5-μm-wide and 1-μm-wide InAsSb layers is shown in Figure 4.3(d). The external efficiency and output power of the LED with the 1-μm-thick active region was almost twice as high as the structures with the 0.5 μm thick active region. This implies that Shockley-Reed-Hall recombination does not control the device current. Data

presented in Figure 4.3(d) are evidence of the fact that the hole diffusion length of the $InAs_{1-x}Sb_x$ layer is of μm scale which is advantageous for LED and photo detector development.

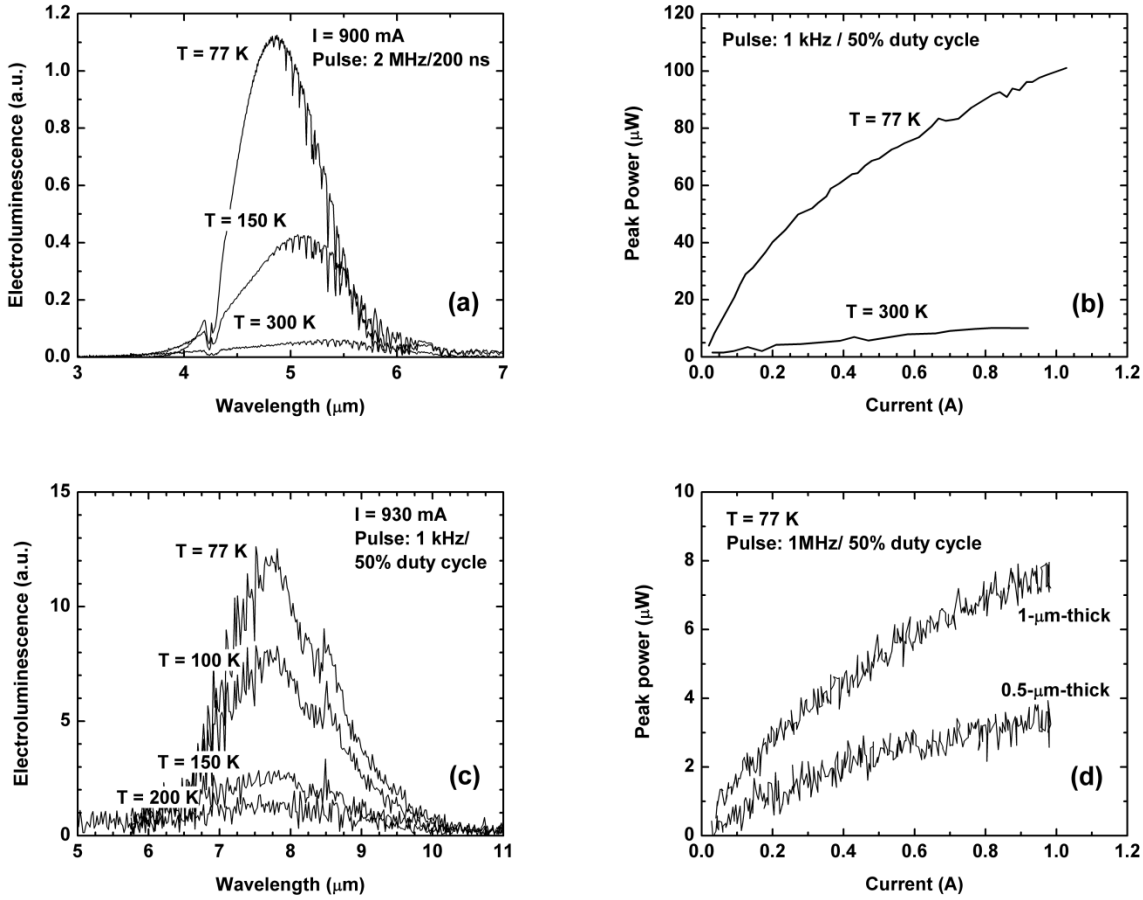

Figure 4.3: Electroluminescence spectra and L-I curves for $InAs_{1-x}Sb_x$ LED with x=0.2 (a, b) and x=0.44 (c, d).

To summarize, we have demonstrated that the growth of GaInSb compositionally graded buffers allows the fabrication of heterostructures containing bulk InAsSb and AlInAsSb layers with lattice constants up to 2.1% larger than that of the GaSb substrate. The 1μm thick $InAs_{0.56}Sb_{0.44}$ layer with an absorption edge above 9 μm (see Fig 3(c)) is characterized by an in-plane residual strain of about 0.08%. The result opens the opportunity to develop heterostructures containing wide-gap barriers and thick (1-3 μm) narrow-gap III-V emitters/absorbers with bandgap energies much lower than that of InSb. These structures with a high interband optical coefficient and excellent transport characteristics are suitable for the

design of IR LEDs, nBn and other types of barrier photodetectors. In the latter case the localization of the electric field exclusively in the barrier area can lead to significant dark current suppression.

4.2 Barrier type photodetectors using bulk InAsSb absorbers

Efficient photodetectors for the spectral range from 8 to 14 μm are required for a variety of applications. In the quest for the most efficient technological solution, photodetector heterostructures based on the III-V family of semiconductors have attracted significant attention for a long period of time. Barrier photodetector designs were recently developed to enhance device performance [21-26]. The generic design targets of the barrier photodetector include: (a) the development of high quality narrow bandgap absorbers with sharp absorption edge and sufficiently high diffusion lengths, and (b) the development of wide bandgap barrier materials with proper band alignment with respect to the absorber section. Although a large range of band gaps and band alignments are available within the III-V materials system, the requirement of high quality growth on commercially available substrates limits the practical design flexibility.

It was shown in Chapter 3 that for InAsSb-based materials utilization of compositionally graded (Al)GaInSb buffer layers can turn the lattice constant into a design parameter. This technology allowed the growth of high quality unstrained unrelaxed InAsSb bulk layers with thickness up to 4 μm on commercially available GaSb substrates. The lattice mismatch of more than 2% between the GaSb substrate and InAsSb alloys having Sb compositions exceeding 40% is effectively accommodated by a network of misfit dislocations confined in the compositionally graded GaInSb buffer layer. It was shown that Te-doped GaInSb relaxed layers do not impede electron transport and thus do not cause any significant voltage penalty in light emitting and laser diodes (as shown in the previous section). Transmission electron microscopy (TEM) studies demonstrated that the density of dislocations threading into the bulk unstrained unrelaxed InAsSb from the GaInSb buffers is below the limit detectable by TEM. It was also confirmed that the optimization of the growth and design parameters allowed the growth of InAsSb bulk layers without any apparent self-ordering [76].

In this work an unstrained and unrelaxed $InAs_{0.6}Sb_{0.4}$ 1-μm-thick bulk layer was gown by MBE on a 3μm thick GaInSb compositionally graded buffer layer and a 500 nm $Ga_{0.66}In_{0.34}Sb$ virtual substrate (similar to that described in Chapter 3). We utilized this layer as the absorber

section of the barrier photodetector. This nominally undoped alloy section demonstrated an absorption edge near 9.5 μm at 77K. Figure 4.4 (a) is a schematic band diagram of the barrier photodetector heterostructure under flat band condition. For the barrier layer we selected a $Al_{0.75}In_{0.25}Sb$ ternary alloy that was lattice matched to $InAs_{0.6}Sb_{0.4}$. The calculation predicted that the large band offset in conduction band between the InAsSb absorber and the AlInSb barrier should suppress the electron transport from the absorber to the n+ InAsSb contact layer. The valence band edges can be expected to be nearly aligned between InAsSb and AlInSb – hence the photo and thermally generated holes can reach the top contact. This idealized picture neglects any effects of possible residual doping in the AlInSb.

To elucidate the effect of the doping type and density of the AlInSb barrier layer on the performance parameters of the barrier photodetectors we produced devices with different intentional doping levels. We compared nominally undoped, with moderately p-doped (Be - 10^{16} cm^{-3}), and heavily p-doped (Be - 10^{17} cm^{-3}) AlInSb. The wafers were processed into front side illuminated devices (Figure 4.4 (b)). We used an inductively coupled $H_2/CH_4/Ar$ plasma reactive ion etching process to define the top contacts into square mesas. A silicon nitride mask was used for mesa definition and the etching process was stopped in the top half of the barrier layer as confirmed by the Scanning Electron Microscopy (SEM) image shown in the inset of Figure 4.4 (b). The mesas were covered by a 300-nm-thick silicon nitride layer followed by the deposition of Ti/Pt/Au contacts. No antireflection coating was applied. The backside contact consisted of an annealed Ni/Au/Ge/Ni/Au layer and a Ti/Pt/Au final metallization.

The quantum efficiency was measured using an 800°C blackbody source with a 2.5 mm aperture at distances from 5 to 30 cm. Figure 4.5 (a) plots the bias dependence of the external quantum efficiency (EQE) at 8 μm measured at 77 K for all three types of devices. A bias of 0.45 V was required for devices with moderately and heavily p-doped barriers to reach saturation of the EQE, while a bias nearly double that was required for devices with nominally undoped barrier layers. Figure 4.5 (b) plots the EQE spectrum at the bias corresponding to saturation. At 77 K more than 10 % efficiency is demonstrated at 8 μm. When the device was heated up to 150 K the bandgap was reduced, shifting the EQE spectrum correspondingly and more than 10 % of EQE was obtained near 9 μm.

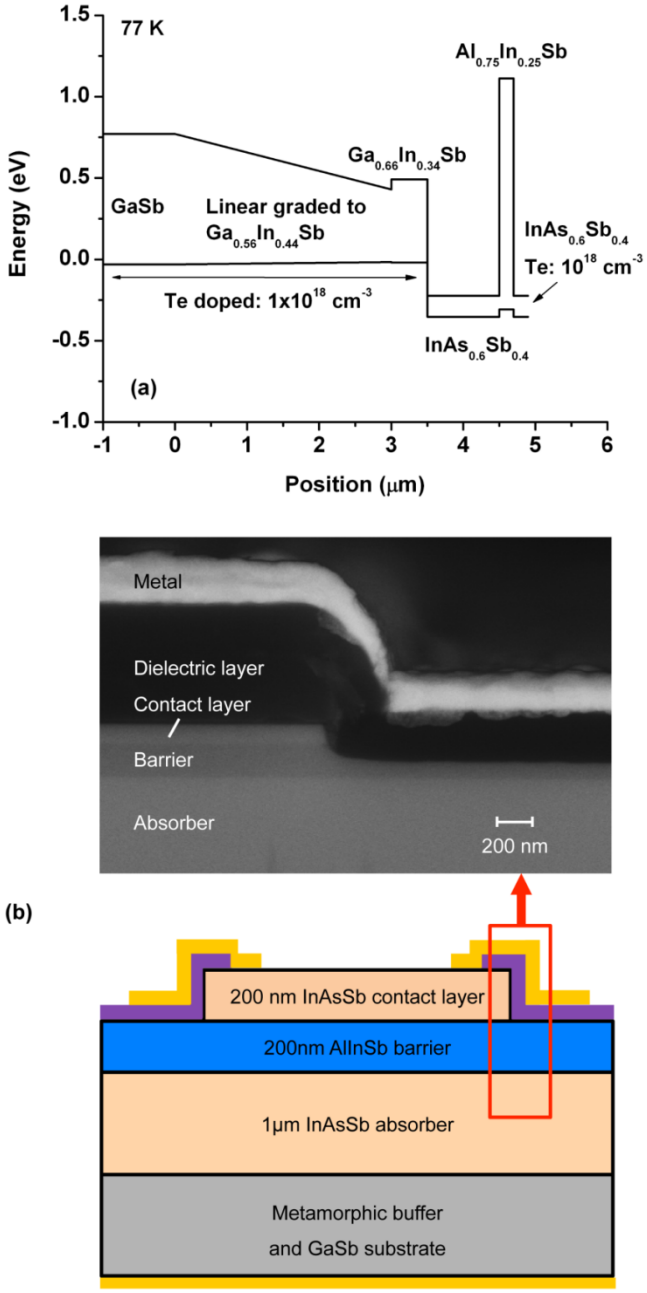

Figure 4.4: (a) Schematic band diagram of the detector heterostructure with undoped InAsSb absorber under flat band condition. The 500 nm $Ga_{0.66}In_{0.34}Sb$ virtual substrate layer is lattice matched to the absorber. No bowing of the valence band offset was assumed. (b) Top: SEM image of the cleaved mesa cross-section; bottom: the schematic structure of the front side illuminated detectors.

The different bias dependence of the EQE efficiency in devices with different p-doping level in AlInSb barrier can be explained as follows. We assume that nominally undoped AlInSb alloys may have a moderate concentration of deep donor centers. In a InAsSb/AlInSb heterostructure these deep donors are ionized and the associated space charge leads to a barrier for diffusion of minority holes into the top contact layer. A further increase of the bias is required for suppression of the barrier due to the modulation doping effect. When residual n-doping is compensated by intentional p-doping, the modulation doping barrier is reduced or even eliminated. Unnecessarily high p-doping of the barrier layer would create a depletion region in the absorber section and/or can cause significant tunneling under bias.

The values of EQE in the 1-μm-thick absorber correspond to an estimated absorption coefficient above 2000 cm^{-1} for photon energies of about 15 meV above the absorption edge (e.g. at the wavelength of 8 μm at 77 K). The high absorption coefficient value is an inherent advantage of the bulk III-V absorber material.

Figure 4.6 plots the dark current-voltage characteristics at 77 K for all three types of devices. The dark current values corresponding to biases required to reach the maximum EQE are nearly the same for devices with nominally undoped and moderately p-doped barrier layers. The device with moderately doped barrier layer has a dark current density of 5×10^{-4} A/cm^2 at a bias voltage of 0.45 V. The estimated specific detectivity of this device at 77 K is about 4×10^{10} $cmHz^{1/2}W^{-1}$. The device with heavily p-doped barrier demonstrates much higher dark current values. This can be explained by the increased contribution of the band-to-band tunneling current and/or appearance of a depletion region in the InAsSb absorber section due to the pn-junction at the n^--InAsSb/p^+-AlInSb interface. The inset in Figure 4.6 plots the temperature dependence of the dark current density (bias is 0.45 V) for a device with a moderately doped barrier layer. In the temperature range above 100 K the activation energy for the dark current density at this bias voltage was equal to 124 meV.

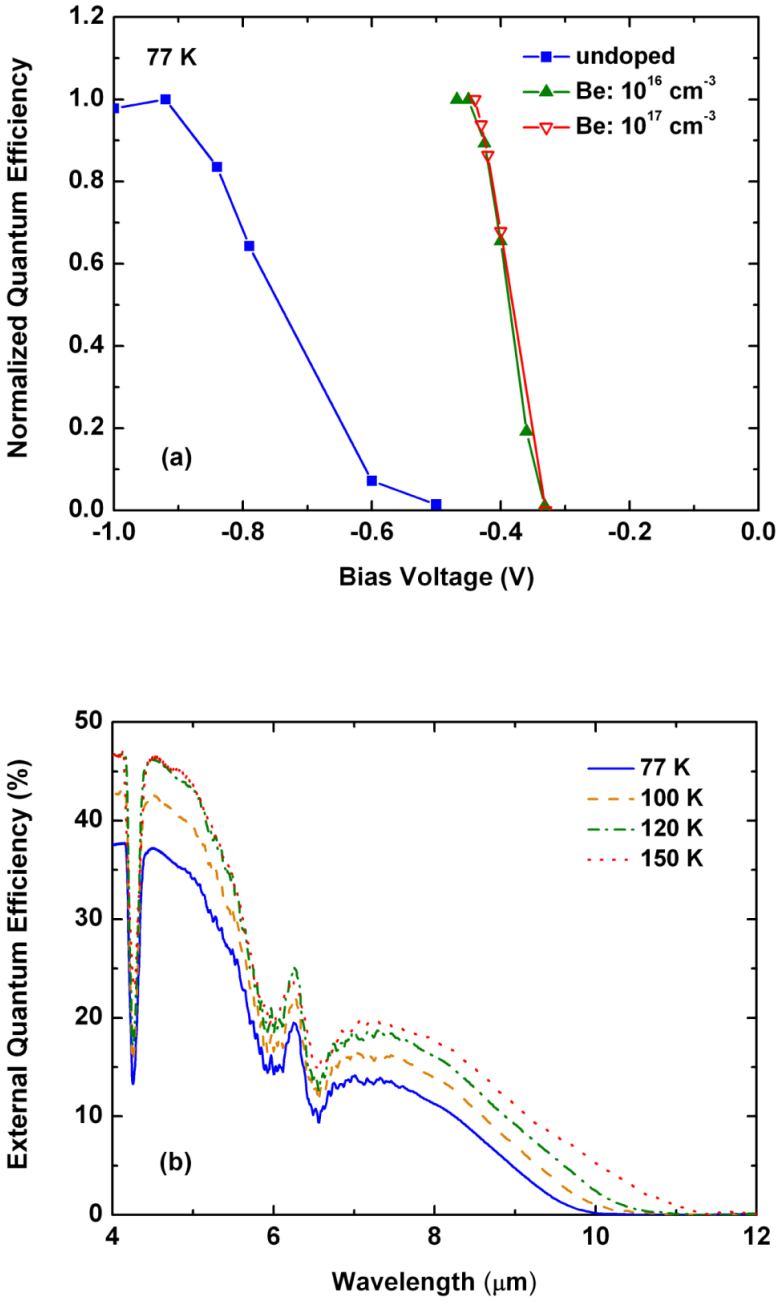

Figure 4.5: (a) The bias dependence of normalized EQE at 8 μm at 77 K for all three types of devices. (b) EQE spectra at biases corresponding to saturation in a temperature range from 77 K to 150 K.

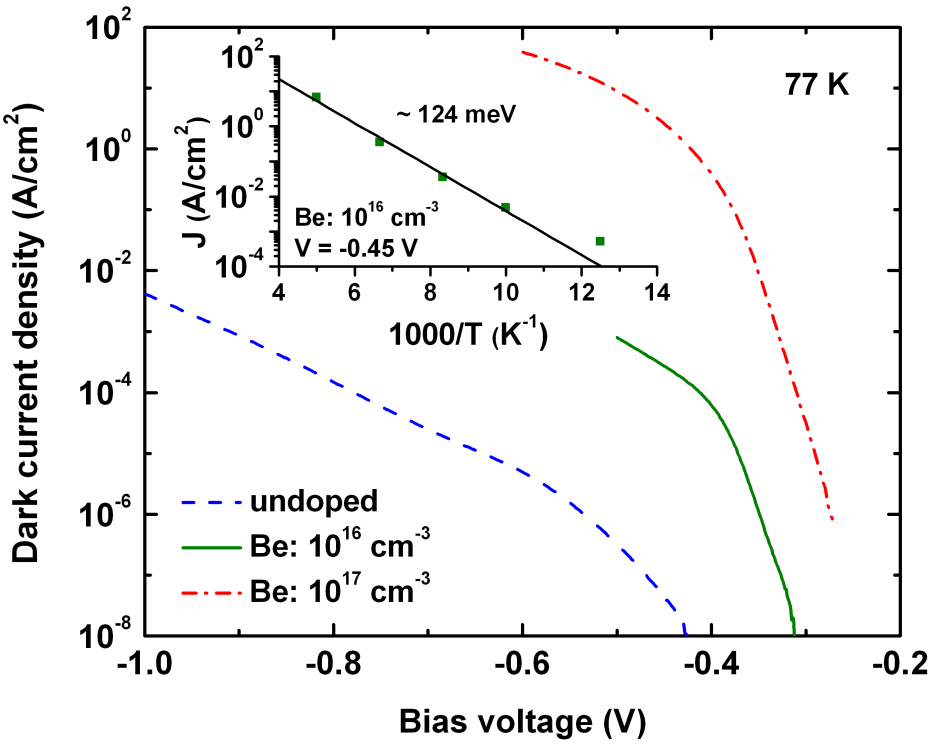

Figure 4.6: Dark current density as a function of bias voltage for all three types of devices at 77 K. Inset: Temperature dependence of the dark current density at 0.45 V bias for the device with moderately doped barrier. The calculated activation energy from 100 K to 200 K is 124 meV.

In summary, long-wave infrared nBn photodetectors with bulk, unrelaxed $InAs_{0.6}Sb_{0.4}$ absorbers, and $Al_{0.75}In_{0.25}Sb$ barriers grown on compositionally-graded GaInSb buffers on GaSb substrates were fabricated by molecular beam epitaxy and characterized. The heterostructures with 1-μm thick absorbers demonstrated external quantum efficiencies of 12 % and 18 % at a bias voltage of 0.45 V and temperatures of T = 77 and 150 K, respectively. The estimated specific detectivity of this device at 77 K is about 4×10^{10} $cmHz^{1/2}W^{-1}$.

Chapter 5 Summary

GaSbN and InAsN bulk materials were grown by MBE with nitrogen contents of up to 1.4% and 2.25% respectively. Transmission experiments show that the absorption edge energy decreases by nearly 300 meV compared to GaSb for the sample with 1.4% nitrogen. The energies of the radiative transitions correlate well with the bandgap energies estimated assuming direct allowed band-to-band optical transitions. The carrier lifetimes in GaSbN determined from a nonlinear up-conversion technique, and assuming linear recombination, decrease from 6-7 ps to 2-3 ps when the nitrogen content is increased from 0.3% to 1.4%. Further studies are required to identify the physical mechanism responsible for the fast carrier relaxation dynamics in dilute-nitride GaSbN bulk materials. Photoluminescence measurements in InAsN show that the bandgap energy decreases continuously from that of InAs by nearly 150 meV when nitrogen content is increased up to 2.25 %. Comprehensive absorption and photoluminescence spectroscopy analysis demonstrates Moss-Burstein shift below 30 meV for nitrogen content of 2 %. The separation of the PL and absorption edge is apparent only at low temperatures and for sample with 2 % of nitrogen. The low excitation minority carrier lifetimes at 78 K decrease from about 8 to about 5 ns when nitrogen content is increased from 1 to 2 %. At elevated temperatures the minority carrier lifetime decreases from 8 to 2.5 ns for nitrogen content of 1 %. More than three orders of magnitude improvement in minority carrier lifetime is observed in unoptimized InAsN material as compared to GaSbN, encouraging further optimization of the former for detector applications. Difference in energetic position of the nitrogen complex states can be responsible for the observed difference.

$InAs_{1-x}Sb_x$ alloys have the smallest bandgap energies within conventional III-V semiconductors. We provided experimental evidence to show that growing compositionally graded buffers (Ga(Al)InSb on GaSb substrates) with a strained but unrelaxed top layer allows the fabrication of high quality bulk $InAs_{1-x}Sb_x$ layers (0.5~1.5 μm thick) with their native lattice parameters. These films have characteristics that are promising for the development of IR detectors operating within the spectral range from 5 to 12 μm. The critical element of the technology is the control of the in-plane lattice constant of the topmost section of the buffer. The in-plane lattice constant of this layer must be equal to the lattice constant of $InAs_{1-x}Sb_x$ with given x. The unrelaxed $InAs_{1-x}Sb_x$ epitaxial layers grown on top of such buffers demonstrated photoluminescence in the spectral range from 5.2 to 9.4 μm within the temperature range of

77~150 K. The carrier lifetime of 250 ns was obtained at T = 77 K for structure consisting $InAs_{0.8}Sb_{0.2}$ epi-layers.

These results open the opportunity to develop heterostructures containing wide-gap barriers and thick (1-3 μm) narrow-gap III-V bulk emitters/absorbers with bandgap energies much lower than that of InSb. These structures can have the advantages of high interband optical coefficient and excellent transport characteristics, and can be suitable for the design of IR LEDs, nBn and other types of barrier photodetectors. Following this further, Light emitting diodes (LEDs) and photodetectors were fabricated using $InAs_{1-x}Sb_x$ alloys. LEDs with x = 0.2 and x = 0.4 demonstrated output powers of 90 μW at 5 μm and 8 μW at 8 μm respectively, at the temperature of 80 K. Barrier type photodetectors with $InAs_{1-x}Sb_x$ (x = 0.4) absorber layer and AlInSb barrier were fabricated. Front side illuminated detectors with 1-μm thick absorber demonstrated external quantum efficiencies of 12 % and 18% at 8 μm at temperature of 77 K and 150 K, respectively. The estimated specific detectivity of this device at 77 K is about 4×10^{10} $cmHz^{1/2}W^{-1}$. Future works in the direction of photodetectors include increasing the thickness of the absorber layer to maximize the absorption, and improving the noise performance to maximize the ability to detect weaker signals.

References

[1] I. Vurgaftman, J. R. Meyer, and L. R. Ram-Mohan, J. Appl. Phys. **89**, 5815 (2001).

[2] G. A. SaiHalasz, R. Tsu, and L. Esaki, Appl. Phys. Lett. **30**, 651 (1977).

[3] I. Vurgaftman, W. W. Bewley, C. L. Canedy, C. S. Kim, M. Kim, C. D. Merritt, J. Abell, J. R. Lindle, and J. R. Meyer, Nature Commun. **2**, 585, (2011).

[4] J. Faist, F. Capasso, D. L. Sivco, C. Sirtori, A. L. Hutchinson, and A. Y. Cho, Science, **264**, 553 (1994).

[5] Courtesy to "http://lamp.tu-graz.ac.at/~hadley/ss1/empty/empty.php"

[6] M. L. Cohen, and T. K. Bergstresser, Phys. Rev. **141**, 789 (1966).

[7] J. C. Slater and G. F. Koster, Phys. Rev. **94**, 1498 (1954).

[8] S. Ben Radhia, N. Fraj, I. Saidi and K. Boujdaria, Semicond. Sci. Technol. **22**, 427 (2007)

[9] E. O. Kane, J. Phys. Chem. Solids **6**, 236 (1958).

[10] G. Belenky, D. Donetsky, G. Kipshidze, D. Wang, L. Shterengas, W.L. Sarney, and S.P. Svensson, Appl. Phys. Lett. **99**, 141116 (2011).

[11] M. Rattunde, J. Schmitz, R. Kiefer, and J. Wagner, Appl. Phys. Lett. **88**, 081115 (2006).

[12] G. Belenky, L. Shterengas, G. Kipshidze, and T. Hosoda, IEEE J. Sel. Top. Quant. Electron. **17**, 1426 (2011).

[13] N. Bandyopadhyay, Y. Bai, S. Tsao, S. Nida, S. Slivken, and M. Razeghi, Appl. Phys. Lett. **101**, 241110 (2012).

[14] F. Capasso, R. Paiella, R. Martini, R. Colombelli, C. Gmachl, T. L. Myers, M. S. Taubman, R. M. Williams, C. G. Bethea, K. Unterrainer, H. Y. Hwang, D. L. Sivco, A. Y. Cho, A. M. Sergent, H. C. Liu, and E. A. Whittaker, IEEE J. .Quant. Electron. **38**, 511 (2002).

[15] C. Cmachl, D. L. Sivco, R. Colombelli, F. Capasso, and A. Y. Cho, Nature, **415**, 883 (2002).

[16] S. Suchalkin, S. Jung, G. Kipshidze, L. Shterengas, T. Hosoda, D. Westerfeld, D. Snyder, and G. Belenky, Appl. Phys. Lett. **93**, 081107 (2008).

[17] R. Q. Yang, C. -H. Lin, S. J. Murry, S. S. Pei, H. C. Liu, M. Buchanan, and E. Dupont, Appl. Phys. Lett. **70**, 2013 (1997).

[18] N. C. Das, J. Bradshaw, F. Towner, R. Leavitt, Solid State Electron. **52**, 1821 (2008).

[19] E. J. Koerperick, J. T. Olesberg, T. F. Boggess, J. L. Hicks, L. S. Wassink, L. M. Muaary, and J. P. Prineas, Appl. Phys. Lett. **92**, 121106 (2008).

[20] E. J. Koerperick, D. T. Norton, J. T. Olesberg, B. V. Olson, J. P. Prineas, and T. F. Boggess, IEEE J. Quant. Electron. **47**, 50 (2011).

[21] S. Maimon and G. W. Wicks, Appl. Phys. Lett. **89**, 151109 (2006).

[22] P. C. Klipstein, Proc. SPIE 6940, Infrared Technology and Applications XXXVIII, 694002U (2008).

[23] D. Z.-Y. Ting, C. J. Hill, A. Soibel, S. A. Keo, J. M. Mumolo, J. Nguyen, and S. D. Gunapala, Appl. Phys. Lett. **95**, 023508 (2009).

[24] B.-M Nguyen, S. Bogdanov, S. Abdollahi Pour, and M. Razeghi, Appl. Phys. Lett. **95**, 183502 (2009).

[25] H. S. Kim, O. O. Cellek, Z.-Y. Lin, Z.-Y. He, X.-H Zhao, S. Liu, H. Li, and Y.-H. Zhang, Appl. Phys. Lett. **101**. 161114 (2012).

[26] N. Gautam, S. Myers, A. V. Barve, B. Klein, E. P. Smith, D. R. Rhiger, H. S. Kim, Z.-B. Tian, S. Krishna, IEEE J. Quant. Electron. **49**, 211 (2013).

[27] M. Weyes, and M. Sata, Appl. Phys. Lett. **62**, 1396 (1993).

[28] T. D. Veal, L. F. J. Piper, P. F. Jefferson, I. Mahboob, C. F. McConville, M. Merrick, T. J. C. Hosea, B. N. Murdin, and M. Hopkinson, Appl. Phys. Lett. **87**, 182114 (2005).

[29] W. Shan, W. Walukiewicz, J. W. Ager III, E. E. Haller, J. F. Geisz, D. J. Friedman, J. M. Olson, and S. R. Kurtz, Phys. Rev. Lett. **82**, 1221 (1999).

[30] A. Belabbes and M. Ferhat, Appl. Phys. Lett. **88**, 152109 (2006).

[31] J. Y. Huang, L. J. Mawst, S. Jha, T. F. Kuech, D. Wang, L. Shterengas, G. Belenky, J. R. Meyer, and I. Vurgaftman, J. Cryst. Growth **310**, 4839 (2008).

[32] K. M. Yu, W. Walukiewicz, J. Wu, J. W. Beeman, J. W. Ager, III, E. E. Haller, W. Shan, H. P. Xin, and C. W. Tu, Appl. Phys. Lett. **78**, 1077 (2001).

[33] B. N. Murdin, M. Kamal-Saadi, A. Lindsay, E. P. O'Reilly, A. R. Adams, G. J. Nott, J. G. Crowder, C. R. Pidgeon, I. V. Bradley, J.-P. R. Wells, T. Burke, A. D. Johnson, and T. Ashley, Appl. Phys. Lett. **78**, 1568 (2001).

[34] P. R. C. Kent, and A. Zunger, Phys. Rev. B **64**, 115208 (2001)

[35] A. Lindsay, E. P. O'Reilly, A. D. Andreev, and T. Ashley, Phys. Rev. B 77, 165205 (2008).

[36] H. T. Pham, S. F. Yoon, K. H. Tan, and D. Boning, Appl. Phys. Lett. **90**, 092115 (2007).

[37] H. P. Nair, A. M. Crook, K.M. Yu, and S. R. Bank, Appl. Phys. Lett. 100, 021103 (2012)

[38] T. D. Veal, L. F. J. Piper, S. Jollands, B. R. Bennett, P. H. Jefferson, B. N. Murdin, L. Buckle, G. W. Smith, and T. Ashley, Appl. Phys. Lett. **87**, 132101 (2005).

[39] P. H. Jefferson, T. D. Veal, L. F. J. Piper, B. R. Bennett, C. F. McConville, B. N. Murdin, L. Buckle, G. W. Smith, and T. Ashley, Appl. Phys. Lett. **89**, 111921 (2006).

[40] W. Li, J. B. Hercux, and W. I. Wang, J. Appl. Phys. **94**, 4248 (2003).

[41] S. Iyer, L. Wu, J. Li, S. Potoczny, K. Matney, and P. R. C, Kent, J. Appl. Phys. **101**, 113508 (2007).

[42] A. Chandola, R. Pino and P. S. Dutta, Semicond. Sci. Technol. **20**, 886 (2005).

[43] P.Y. Yu, M. Cardona, *Fundamentals of Semiconductors*, *the third edition*, ISBN 3-540-41323-5, Springer-Verlag (2001).

[44] I. Vurgaftman and J. R. Meyer, J. Appl. Phys. **94**, 3675 (2003).

[45] J. Shah, "Ultrafast luminescence spectroscopy using sum frequency generation", IEEE J. Quantum Electron. **24**, 276 (1988).

[46] D.-K. Shih, H.-H. Lin, L.-W. Sung, T.-Y. Chu, and T.-R. Yang, J. J. Appl. Phys. **42**, 375 (2003).

[47] T. Ashley, T.M. Burke, G.J. Pryce, A.R. Adams, A.D. Andreev, B.N. Murdin, E.P. O'Reilly, Solid State Electron. **47**, 387 (2003).

[48] A. Rogalski, New ternary alloy system for infrared detectors, SPIE, Washington, 1994.

[49] L. Shterengas, G. Belenky, J.-Y. Yeh, L.J. Mawst, N. Tansu, J. Sel. Top. Quant. Electron. **11**, 1063 (2005).

[50] W. Ha, V. Gambin, S. Bank, M. Wistey, H. Yuen, S. Kim, J. S. Harris, IEEE J. Quant. Electron. **38**, 1260 (2002).

[51] Q. Zhuang, A. Godenir, A. Krier, G. Tsai, and H. H. Lin, Appl. Phys. Lett. **93**, 121903 (2008).

[52] M. Merrick, S. A. Cripps, B. N. Murdin, T. J. C Hosea, T. D. Veal, C. F. McConville, M. Hopkinson, Phys. Rev. B **76**, 075209 (2007).

[53]Q. Zhuang, A.M.R. Godenir, A. Krier, K.T. Lai, S.K. Haywood, J. Appl. Phys. **103**, 063520 (2008).

[54] A. Patane, W. H. M. Feu, O. Makarovsky, O. Drachenko, L. Eaves, A. Krier, Q. D. Zhuang, M. Helm, M. Goiran, G. Hill, Phys. Rev. B **80**, 115207 (2009).

[55] Y. Lacroix, C.A. Tran, S.P. Watkins, M.L.W. Thewalt, J. Appl. Phys. **80**, 6416 (1996).

[56] The two-level BAC model was calculated using parameters for InNAs alloys: 1.44 eV for nitrogen resonant state and 2.5 eV for the interaction potential at 12 K as taken from [52].

[57] D. J. Jang, M. Flatte, C. H. Grein, J. T. Olesberg, T. C. Hasenberg, T. F. Bogges, Phys. Rev. B **58**, 13047 (1998).

[58] L. Shterengas, G. L. Belenky, J. G. Kim and R. U. Martinelli, Semicond. Sci. Tech., **19**, 655 (2004).

[59] J. Tersoff, Appl. Phys. Lett., **62**, 693 (1993).

[60] G. Kipshidze, T. Hosoda, W. L. Sarney, L. Shterengas, and G. Belenky, IEEE Photon. Technol. Lett. **23**, 317 (2011).

[61] M. Y. Yen, R. People, and K. W. Wecht, J. Appl. Phys. **64**, 952 (1988).

[62] Z. M. Fang, K. Y. Ma, D. H. Jaw, R. M. Cohen, and G. B. Stringfellow, J. Appl. Phys. **67**, 7034 (1990).

[63] S. R. Kurtz, L. R. Dawson, R. M. Biefeld, D. M. Follstaedt, and B. L.Doyle, Phys. Rev. B **46**, 1909 (1992).

[64] T.-Y. Seong, G. R. Booker, A. G. Norman, and I. T. Ferguson, Appl. Phys.Lett. **64**, 3593 (1994).

[65] J. D. Kim, D. Wu, J. Wojkowski, J. Poitrovski, J. Xu, and M. Razeghi, Appl. Phys. Lett. **68**, 99 (1996).

[66] S. Nakamura, P. Jayavel, Y. Kobayashi, K. Arafune, T. Koyama, M. Kumagawa, and Y. Hayakawa, Semicond. Sci. Technol. **20**, 1064 (2005).

[67] D. Donetsky, S. P. Svensson, L. E. Vorobjev, and G. Belenky, Appl. Phys. Lett. **95**, 212104 (2009).

[68] J. G. Crowder, H. R. Hardaway, and C. T. Elliott, Meas. Sci.Technol. **13**, 882–4 (2002).

[69] N. V. Zotova, N. D. Il'inskaya, S. A. Karandashev, B. A. Matveev, M. A. Remennyi, and N. M. Stus', Semiconductors, **40**, 697-703 (2006).

[70] See, e.g., A. Rogalski, and K. Chrzanowski, Opto-Electron. Rev., **10**, 111-136 (2002)

[71] D. Donetsky, G. Belenky, S.P. Svensson, and S. Suchalkin, Appl. Phys. Lett. **97**, 052108 (2010).

[72] E.H. Steenbergen, B.C. Connelly, G.D. Metcalfe, H. Shen, M. Wraback, D. Lubyshev, Y. Qiu, J.M. Fastenau, A.W.K. Liu, S. Elhamri, O.O. Cellek and Y.-H. Zhang, Appl. Phys. Lett. **99**, 251110 (2011).

[73] D. Lackner, M. Steger, M.L.W. Thewalt, O.J. Pitts, Y.T. Cherng, S.P. Watkins, E. Plis, and S. Krishna, J. Appl. Phys. **111**, 034507 (2012).

[74] E.H. Steenbergen, K. Nunna, L. Ouyang, B. Ullrich, D.L. Huffaker, D.J. Smith, and Y.-H. Zhang, J. Vac. Sci. Technol. B **30**, 02B107 (2012).

[75] A. Rogalski, *Infrared Detectors, 2nd edition* (CRC Press, Boca Raton, 2011), p.341.

[76] S. P. Svensson, W. L. Sarney, H. Hier, Y. Lin, D. Wang, D. Donetsky, L. Shterengas, G. Kipshidze and G. Belenky, Phys. Rev. B **86**, 245205 (2012).

[77] D. Wang, Y. Lin, D. Donetsky, L. Shterengas, G. Kipshidze, G. Belenky, W. L. Sarney, H. Hier and S. P. Svensson, Proc. SPIE 8353, Infrared Technology and Applications XXXVIII, 835312 (May 1, 2012).

[78] G. Kipshidze, T. Hosoda, W. L. Sarney, L. Shterengas and G. Belenky, IEEE Photon. Tech. Lett. **23**, 317-319 (2011).

[79] U. Pietsch, V. Holy and T. Baumbach, *High-Resolution X-Ray Scattering: From Thin Films to Lateral Nanostructures, 2nd edition* (Springer-Verlag New York, New York, 2004), p.180.